UNIVERSIDAD DE CONCEPCIÓN
FACULTAD DE CIENCIAS FÍSICAS Y MATEMÁTICAS
MAGÍSTER EN CIENCIAS CON MENCIÓN EN FÍSICAS

TESIS

EFFECTS OF THE INITIAL MASS FUNCTION ON THE INFANT MORTALITY OF EMBEDDED STAR CLUSTERS

Matias Andrés Blaña Díaz

Profesor: Dr. Michael Fellhauer

Departamento de Astronomía
Facultad de Ciencias Físicas y Matemáticas
Universidad de Concepción

Concepción, Chile
Agosto 2013

Thesis:
Effects of the Initial Mass Function on the Infant Mortality of Embedded Star Clusters
Magister en Ciencias, mención en Física

Student: *Matias Andrés Blaña Díaz*[1] [*];

Evaluating committee:

Supervising Professor *Dr. Michael Fellhauer*[1] [†]

Professor *Dr. Neil Nagar* [1] [‡]

and

Professor *Dr. Sandro Villanova* [1] [§]

[1] Departamento de Astronomía, Universidad de Concepción, Concepción, Chile

August 2, 2013

[*]E-mail: mblana@astro-udec.cl
[†]mfellhauer@astro-udec.cl
[‡]nagar@astro-udec.cl
[§]svillanova@astro-udec.cl

Resumen

Casi todas las estrellas nacen en cúmulos estelares, y sin embargo la mayoría ya no son parte de uno. Se ha observado un gran número de cúmulos estelares jóvenes que contrasta con la baja cantidad de cúmulos viejos. Esta ausencia de cúmulos viejos implica que algunos mecanismos están destruyendo a los cúmulos en su juventud, un fenómeno llamado *Mortalidad Infantil*. La lista de estos mecanismos es larga: evaporación, disrupción de mareas, etc. Un candidato favorito es la fuerte perturbaci´n que genera la expulsión del gas remanente de un cúmulo estelar recién formado. Simulaciones numéricas muestran que la Tasa de Formación Estelar (o en Inglés: Star Formation Efficiency SFE) es un buen parámetro para estimar la capacidad de sobrevivir que tienen los cúmulos a la expulsión del gas. El cúmulos sobreviviente es cuantificado mediante su masa final que esta gravitacionalmente unida, por medio de la fracción de masa (o en Inglés: final bound fraction $f_{\rm bound}$). Estas simulaciones fueron realizadasbajo la asunción de equilibrio virial y una distribución suave para las estrellas, mostrando que un cúmulo inmerso en su nube de gas con una SFE $= 0.2$ bajo una pérdida rápida de gas no sobreviría a la expulsión del gas. Sin embargo, en simulaciones con distribuciones inicialmente aglomeradas y fuera de equilibrio virial pudo obtenerse cúmulos sobrevivientes (Smith et al. (2012)). Los autores introducen un nuevo parámetro, la Fracción Estelar Local (o en Inglés: Local Stellar Fraction LSF) y obtienen una nueva relación que ayuda a predecir la capacidad de sobrevivencia en cúmulos estelares. Farias et al. (in prep.) encuentra una relación o tendencia entre la fraccón de masa final $f_{\rm bound}$ y el LSF cuando proporción o tasa virial al momento de la expulsión del gas es $Q_{\rm f} = 0.5$. Todos estos estudios fueron hechos con estrellas de igual masa.
En este proyecto exploramos cmo la introducción de una Función de Masa Inicial (o en Inglés Initial Mass Function IMF) afecta el comportamiento y los resultados encontrados previamente para cúmulos con estrellas de igual masa. Para ello analizamos siete casos donde configuramos diversos paramámetros: la Tasa de Formaci ón Estelar, las tasas viriales inicial y final, las muestras de distribuciones IMF, las distribuciones espaciales fractales, y el posicionamiento inicial de las estrellas en cada distribución fractal. Encontramos que la tendencia o relación encontrado para los modelos con estrellas de igual masa permanece aún válida con ciertas consideraciones.

Para bajas concentraciones (bajo LSF) la relación se comporta de forma similar a las simulaciones de igual masa. Para altas concentraciones (alto LSF) la fracción de masa a 15 Myr is dispersado a valores menores que los valores esperados para las simulaciones con estrellas de igual masa. De nuestro análisis de la dependencia en el tiempo de la fracción de masa, vemos que mientras el tiempo avanza, la evolución dinámica interna del cúmulo se vuelve más importante. Para altos LSF (mayor que 0.6) la fracción de masa decae rápidamente en el tiempo y se desvía de la relación para estrellas de igual masa. Mientras que la fracción de masa para simulaciones con estrellas de igual masa permanece casi constante en el tiempo, las simulaciones con una muestra de estrellas IMF muestran a altas LSF una caída de aproximadamente ~ 30 % para la fracción de masa luego de 15 Myr de evolución.

Cuando medimos la fracción de masa a tiempos más tempranos, ~ 3 Myr y ~ 4.5 Myr las diferencias con la relación para estrellas de igual masa disminuyen. Esta diferencia es

mayormente generada por la evolución dinámica del cúmulo remanente luego de la expulsión del gas. La introducción de estrellas con distintas masas incrementa el efecto de diversos mecanismos, como la "evaporación" del cúmulo, y gatilla otros nuevos como la segregación de masa de las estrellas.

Tabién notamos que el posicionamiento aleatorio de las estrellas en la distribución fractal actúa como un parámetro de segundo orden en importancia para cambiar los resultados de las simulaciones con estrellas de igual masa, y este introduce un nuevo factor estocástico en los resultados. Sin embargo cuando medimos la fracción de masa justo luego de la expulsión del gas, la relación general para estrellas de igual masa aun es válida.

También concluimos que la distribución IMF es más importante cuando la concentración del cúmulo es alta (alta LSF) y el cúmulo tiene suficiente tiempo para perder estrellas por medio de la "evaporación". La pérdida de masa estelar por evaporación disminuye la fracción de masa por debajo de la ralacion para estrellas de igual masa. La distribuci'on IMF se vuelve más importante cuando el posicionamiento inicial de las estrellas tiene una configuración de una segregación de masa inicial o primordial. Un cúmulo con estrellas inicialmente segregadas por su masa incrementa su concentración, incrementando su fracción de masa final. Sin embargo cuando la concentración del cúmulo es muy alta, la evaporación que actúa sobre este luego de la expulsión del gas decrementa fuertemente la fracción de masa con el tiempo. Si usamos una segregación inicial de masas "inversa" para un cúmulo, es decir con las estrellas menos masivas en el centro del cúmulo y las más masivas en la perisferia, vemos que el cúmulo no tiene muchas probabilidades de sobrevivir. Así, vemos que la segreacion de masa influye en el valor de LSF al momento de la expulsion del gas pero aún siguiendo la relación para estrellas de igual masa.

Abstract

Allmost all stars are born in star clusters, and yet almost all stars are no longer part of them. A high number of young star clusters are observed in contrast to very few old ones. This absence of old clusters imply that some mechanisms are destroying the clusters in their youth, a phenomenon called *Infant Mortality*. The list of these mechanisms is long: evaporation, tidal disruption, etc. A favorite candidate is the strong perturbation that is generated by the expulsion of the remaining gas from the newly formed star cluster. Numerical simulations show that the Star Formation Efficiency is a good parameter to estimate the survivability of a cluster to the expulsion of the gas. The surviving cluster is quantified with its final gravitationally bound mass through the final bound fraction $f_{\rm bound}$. These simulations were are obtained under the assumption of virial equilibrium and a smooth distribution for the stars, and showing that an embedded star cluster with a SFE $= 0.2$ under a rapid mass loss rate for the gas would not survive. Simulations with initially clumpy and out of equilibrium distributions result in surviving clusters for SFE $= 0.2$ (Smith et al. (2012)). They introduce later the Local Stellar Fraction (LSF) and find new relations that helps to predict the survivability of star clusters. Farias et al. (in prep.) find a trend between the final bound fraction and the LSF when the virial ratio at the moment of gas expulsion is $Q_{\rm f} = 0.5$. All these studies were made with equal-mass stars.

In this project we explore how the introduction of an Initial Mass Function affects the behaviour and results previously found for clusters with equal mass stars. For that we analyse seven cases with the following parameters: the Local Stellar Fraction, the initial and final virial ratio, the samples of IMF distributions, the initial spatial fractal distribution, and the initial spatial positioning of the stars with different masses within the cluster. We find that the trend between the final bound fraction and the LSF at $Q_{\rm f} = 0.5$ found for the models with equal mass stars remains valid within certain considerations.

For low concentrations (low LSF) the results for the bound fraction follow the trend for equal-mass simulations. For high concentrations (high LSF) the bound fraction at 15 Myr is scattered at values lower than those expected for equal mass simulations. From our analysis of the time dependence of the bound fraction we see that as time advances, the internal dynamical evolution of the cluster becomes more important. For high LSF (larger than 0.6) the bound fraction drops very fast with time and deviate from the trend for equal mass stars. While the bound fraction for equal mass simulations remains almost constant with time, the simulations with an IMF sample show at high LSF a drop of $\sim 30\%$ of their bound fraction after 15 Myr of evolution.

When we measure the bound fraction at early times, ~ 3 Myr and ~ 4.5 Myr, the difference with the equal mass trend is reduced. This difference is mostly generated by the internal dynamical evolution of the remaining cluster after the expulsion of the gas. The introduction of stars with different masses increases the effects of several mechanisms like the cluster's 'evaporation' and triggers new ones like mass-segregation.

We also note that the random initial positioning of the masses introduces another factor of stochasticity in the results. It acts like a parameter less important in changing the results for equal mass stars and it . Nontheless when we measure the bound fraction just after the

gas expulsion the general trend for equal-mass simulations is still valid.

We also conclude that the IMF distribution becomes more important when the concentration of the cluster is high (high LSF) and the cluster has enough time to lose stars through 'evaporation'. The stellar mass loss due to evaporation decreases the bound fraction, shifting the values below the trend found for equal mass particles. The IMF distribution also becomes important when the initial positioning of the stars has a configuration with a primordial or initial mass segregation. An initially mass segregated cluster increases the concentration of the cluster, thereby increasing the final bound fraction. Nonetheless, when the concentration is too high, the "evaporation" acting on the cluster before and after the gas expulsion strongly decreases the bound fraction with time. If we use the inverse mass-segregated distributions we see that the cluster has almost no chance to survive at all. So, the mass-segregation influences the resulting LSF at the time of gas-expulsion but still follows the trend for the equal-mass simulations.

Contents

CHAPTER I
Effects of the Initial Mass Function on the Infant Mortality of Embedded Star Clusters

1 Introduction to Star Clusters

1.1 Types of Star Clusters

Star clusters are basically groups of stars. They are an excellent laboratory to test theories of stellar evolution and stellar dynamics, amongst others. They are also used as tools, for example as distance calibrators. Several types of star clusters have been observed, and are classified by their properties like the total mass, number of stars, age, chemical abundances, dynamical states and many others. The most important types are: Globular Clusters, Open Clusters, T-associations, OB-associations, and Embedded Clusters.

Globular Clusters (GC) are generally the most massive clusters and the oldest systems, with stars of ~ 11 Gyr or older. The Milky Way's (MW) GCs are distributed in the halo of the Galaxy and also in the central part. Their masses range from a few ~ 100 $M_\odot$ to very massive ones like 47 Tucanae (shown in the left panel of Fig.1) with $\sim 7 \times 10^5$ $M_\odot$, millions of stars and a tidal radius of ~ 56 pc (Harris W. E., 1996).

Figure 1: *Left panel*: Image of the Globular Cluster 47 Tucanae taken by the Southern African Large Telescope (SALT). *Right panel*: Image of the Open Cluster Pleiades.

Open Clusters (OC) are usually less massive than most GCs and their stars are much younger (less than 1 Gyr). These systems are dense enough to remain gravitationally bound and the ones observed in the MW are distributed mostly in the disc where the Giant Molecular Clouds and the star formation regions are. In the right panel of Fig.1 we show The Pleiades, a young Open Cluster of around 75 to 100 Myr years. It has 7 bright massive blue B-type stars, and more than a thousand less massive stars. This proportion between high mass stars and low mass stars is the result of a mass distribution for the stars in clusters

that is apparently universal . According to this mass-distribution, called the Initial Mass Function (IMF), clusters initially are constituted by lots of low mass stars, and very few high mass stars. Then, according to stellar evolution, the massive stars would rapidly turn to supernovae, leaving only the low mass stars. Later in Sec.2.6 we discuss the current IMF models.

OB-associations are very young and low mass star clusters with several thousand star members, and characterized by having massive O and B type stars. These massive stars are the source of strong stellar winds and UV radiation that ionizes the parent molecular cloud. Contrary to GCs or OCs, these systems are gravitationally unbound.

T-associations consist mostly of T Tauri stars which are in the pre-main-sequence phase of evolution. These associations are one of the smallest populations in number and size, containing only a few hundreds of stars and have a low total mass.

Statistically speaking, only 10% of all stars have been part of an Open Cluster (Adams & Myers, 2001), the other 90% spend their youth in OB or T associations (Stahler, 2012).

Embedded Clusters (ECL) are forming or just formed star clusters which are still embedded within their primordial Giant Molecular Cloud (GMC).

1.2 Formation of Star Clusters

Almost all stars are formed in stars clusters (Bressert et al., 2012) from a parent GMC where they stay embedded until the expulsion of the gas happens. The MW's GMCs are distributed in the disc of the Galaxy and they are the factories of stars. The rate of production or Star Formation Rate (SFR) for a spiral galaxy like the MW is 1.9 ± 0.4 $M_{\odot}\,yr^{-1}$ (Chomiuk and Povich, 2011). Most of the embedded clusters ($\sim 90\%$) are low mass systems, with populations from a few hundreds to thousands of stars (Lada & Lada, 2003). If we now focus on the low mass star clusters (few hundred solar masses) and analyse their age, we see that there are very few clusters older than 15 Myr. After only 10-20 Myr the majority of stars are dispersed into the field (Lada & Lada, 2003).

The destruction of the young star clusters has been named 'Infant Mortality'. There are several mechanism that conspire to destroy star clusters. The best candidate to explain this early destruction is attributed to the expulsion of the remaining gas of the primordial giant molecular cloud which is driven by stellar feedback through radiation, stellar winds and finally by the first supernovae explosions.

GMCs are rich in dust, making the stars within the cloud only visible at infrared wavelengths. In Fig.2 (Lada & Lada, 2003) we show an example, the Trapezium embedded Open Cluster located almost in the centre of the Orion Nebula. Giant molecular clouds turn only a few tens per cent of their gas into stars (Lada & Lada, 2003) and this is quantified by the star formation efficiency (SFE), which is the ratio between mass converted into stars and total mass of the star forming region (stars + gas). Therefore the gravitational potential of the embedded star cluster (star cluster which is still within its gas-cloud) is dominated by the remaining gas and the expulsion of this gas will leave the stars of the cluster in an out-of-equilibrium dynamical state. This process has been studied theoretically by various groups (Hills (1980), Elmegreen & Clemens (1985), Goodwin (1997a), Goodwin (1997b), Geyer

& Burkert (2001), Boily & Kroupa (2003a), Boily & Kroupa (2003b), Bastian & Goodwin (2006), Baumgardt and Kroupa (2007), Parmentier et al. (2008), Goodwin (2009) and many more).

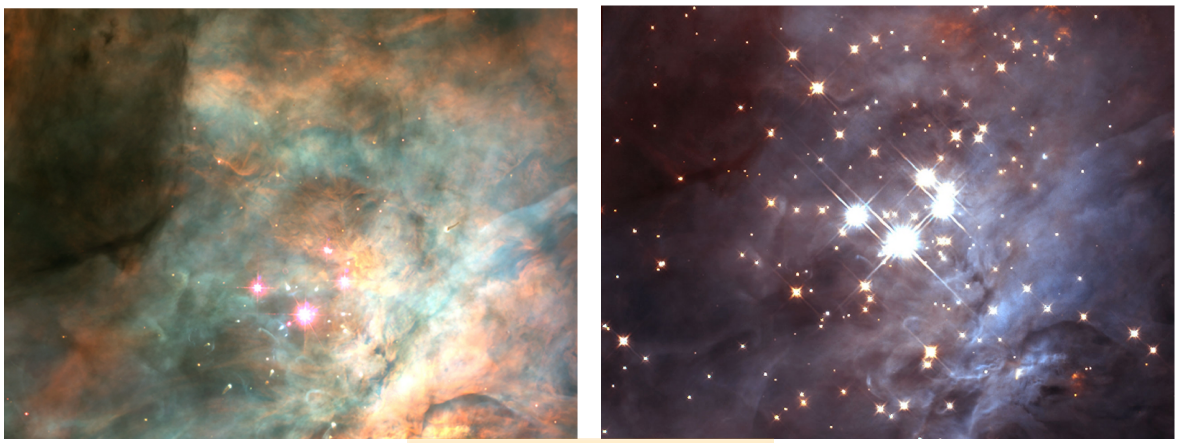

Figure 2: From Lada & Lada (2003), the Trapezium cluster shown in different wavelengths. *Left panel*: Image in the optical band. The dust blocks most of the light in this range of the spectrum, hidding the stars in the centre. *Right panel*: image in the infra red band showing massive stars in the centre, surrounded by less massive stars.

In most of these studies is assumed that at the moment of the gas-expulsion of the embedded star cluster, the system is in virial equilibrium, forming a spherically distribution of stars. Under these assumptions all studies agree that to obtain a surviving bound remnant star cluster after the expulsion of the gas, the SFE has to be at least of 30 per cent and/or the gas-expulsion has to be very slow. This would explain the 'infant mortality' of star clusters, and why the majority of stars are found as field stars. This would imply that with the observed SFE in embedded clusters (less than 30 per cent) we should see even less surviving star clusters than we actually detect.

Recent observations of embedded star forming regions (e.g. Elmegreen & Elmegreen (2001), Gutermuth et al. (2009), Bressert et al. (2012)) show that stars do not form in spherical distributions, nor in virial equilibrium. Instead they form arranged in clumpy and filamentary structures, and most likely dynamically cool (sub-virial) as seen in Fig.3 (*left panel*), where we show the Perseus molecular cloud complex, the Taurus-Auriga molecular cloud complex, and the Orion star forming region (T. Preibisch). The same result is found in gravo-turbulent models of collapsing gas clouds (e.g.Klessen (1997), Mac Low (1999), Bonnell and Bate (2006), Bonnell et al. (2011), Bate (2009), Bate (2011)). Here supersonic turbulence drives the gas to fragment and form dense clumps and filaments, in which the stars are born. In Fig.3 (*right panel*) we show the simulation performed by Bate (2009), which consists of a $2500\ \mathrm{M}_{\odot}$ distribution of turbulent gas constantly forming stars.

These strongly non-equilibrium initial conditions play a crucial rôle in how the gas-expulsion affects the evolution of the cluster. A key factor in determining the effect of the

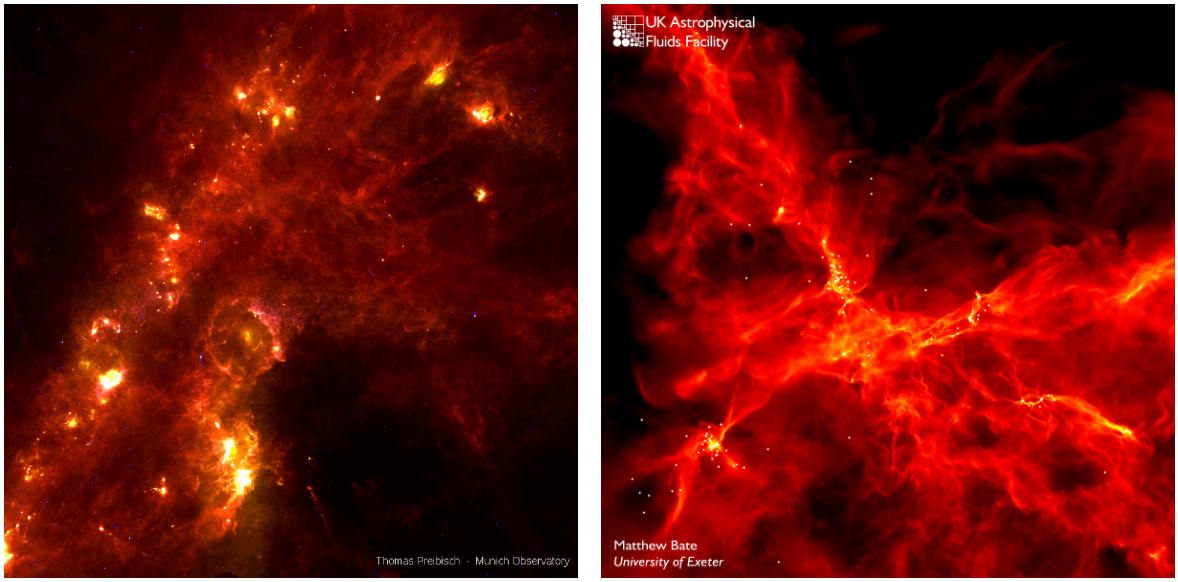

Figure 3: *Left panel*: a very large field of the sky (some 100 x 100 square-degrees) including the Perseus molecular cloud complex (upper right), the Taurus-Auriga molecular cloud complex (upper left), and the Orion star forming region (lower center) 12 micrometer radiation is shown in blue, 60 micrometer in green, and 100 micrometer in red. *Right panel*: Simulation of Bate (2009) of a star cluster forming from a Molecular Cloud. The snapshot correspond to 0.190 Myr and the whole process takes less than 0.5 Myr.

gas expulsion is not only the amount and concentration of the gas (i.e. the depth of the gas gravitational potential), but also the dynamical state of the star cluster at the moment of gas expulsion (e.g.Verschueren and David (1989), Goodwin (2009)). This has led to the development of models of low mass embedded star clusters ($\sim$ 500 $M_{\odot}$) in which a dynamically cool and clumpy initial state collapses and violently relaxes into a more dense star cluster (e.g.Farias et al. (in prep.), Smith et al. (2012), Fellhauer et al. (2009), Allison et al. (2009), Allison et al. (2010)). Therefore we expect that the survival of star clusters to gas-expulsion does not depend only on the global SFE. It will also heavily depend on the clumpy, non-symmetrical distribution at the time of gas-expulsion, and the virial state the stars are in.

Fellhauer et al. (2009) and Smith et al. (2011) explore how fast sub-structure is erased in an initially clumpy distribution, depending on the strength of the gas potential and the distribution of the clumps. These studies suggest that most of the sub-structure is erased quite fast, after only a few crossing-times of the cluster, but some structural and dynamical irregularities survive, influencing the survival of the clusters, as shown by the bound fraction after the gas-expulsion. The highly idealized models described above at the moment of gas-expulsion would not represent the most frequent dynamical state in star clusters, as the distribution of stars have changed and are completely different to their initial conditions. The simulations

done by Smith et al. (2011) under these initial conditions obtain several surviving bound clusters using a SFE $= 0.2$. This means that the global initial parameters, such as the SFE, do not well describe the system any longer. Smith et al. (2011) propose another parameter that uses the ratio between the mass in stars and the total mass measured within the central region of the cluster, the 'Local Stellar Fraction' (LSF). This parameter demonstrated to be a much better indicator of cluster survival, obtaining a clear relation between the LSF and the final bound mass of the remaining cluster. Their simulations show oscillations around virial equilibrium and these deviations add an extra scatter to the final results. The remaining substructure and the small scale deviations from virial equilibrium decay with time, after several crossing-times of the star cluster. However, if gas-expulsion occurs early, a significant scatter appears, which means that the survival of *individual* embedded clusters to gas expulsion is very difficult to predict (Smith et al. 2012). Only by running many different random realizations can we gain some statistical insight into the final result - something achievable on reasonable timescales only with rather idealized models. In this sense, idealized models are indispensable tools.

Current models studying these processes are either idealized as well, or lack the exact treatment of the stellar dynamics, or alternatively are extremely time consuming. In the latter case, it is thus impossible to obtain statistically significant results, given the inherent scatter we have seen when using clumpy distributions of stars. In this research we want to continue our successful research using our fast idealized models. We make use of a cutting-edge N-body code (NBODY 6 Aarseth 2003) to treat the stellar dynamics of the stars with high precision, including close encounters, binaries and multiples.

The gas-phase is treated as an analytical potential (a Plummer distribution and a uniform sphere), which gets removed according to a certain recipe (either instantaneously or declining in a $1/t$ manner) after a defined delay-time. We emphasize our consistent use of clumpy initial stellar distributions. This is much more realistic, and matches the observed and modeled distributions of young stellar objects in embedded star forming regions. This is a great improvement to modeling them as a smooth, relaxed, spherically symmetric star cluster. To mimic the clumpiness of the stellar distribution we use stars distributed in fractal distributions. The initial virial state of the stars is also poorly constrained and so we vary the initial virial state of the stars from strongly sub-virial to virial. In our previous models we used a standard, dense proto star cluster as initial conditions. These studies (Smith et al. 2011a, 2012), and those of our international collaborators (Allison et al. 2009, 2010), have demonstrated that more realistic, clumpy initial stellar distributions can result in highly differing final results, just using different random realizations, even when global parameters have been kept constant. Therefore, any single simulation cannot be used to predict the way an embedded star cluster will evolve. It is therefore necessary to draw conclusions in a broad statistical manner, running dozens or even hundreds of different random realizations of the same parameter set. As our models run fast, this is achievable. With this project we want to first broaden our statistical data-base of possible outcomes. The findings we obtain have to be verified in different environments, i.e. we want to vary the size and density of our star forming region to assess the influence of those main global parameters. It is vital to quantify the intrinsic stochastic scatter. It may be that we will never be able to predict the survival of

one individual embedded cluster. However, for numerous embedded star clusters, we could provide overall statistics for cluster survival, and fractions of stars freed to become field stars. We could then understand the rôle of the numerous star forming regions inside a star forming galaxy, like the Milky Way, for shaping the galaxy morphology as a whole.

The previous models were also highly idealized as they had no mass-spectrum for the stars and no initial binaries. We have, so far, purposely neglected these in order to study the 'pure' influence of the clumpiness. In this way, we avoid the 'kitchen-sink' approach in which all physical processes are included at once and an understanding of the rôle of each process is confused and clouded. Furthermore, these fully hydrodynamical models include multiple ad-hoc recipes for complex physics, such as e.g. stellar feedback, which may be poor descriptions of reality. Instead, we want to increase the complexity of our models step by step in order to assess the influence of each parameter individually on our results. By this approach, we aim to gain a clear understanding of the rôle of each process on cluster survival.

1.3 A New Parameter: The Initial Mass Function

In previous investigations done by Smith et al. (2012) and Farias et al. (in prep.) the models to study the infant mortality are made with equal mass stars. Nonetheless, when the stars of a cluster form in a GMC, their masses follow a density distribution function, called the Initial Mass Function (IMF) which is characterized by having many low mass stars and very few high mass stars (Kroupa, 2001). We later discuss in more detail the properties of this function. The central task in this project is the introduction of the IMF in our simulations, which gives different masses to the stars. We are interested in analazing the dynamical evolution of the cluster with this new initial conditions. There are several new dynamical mechanisms like the spatial segregation of the stars by their masses, that play an important rôle in the clusters survival.

We also study the importance of initial mass segregation (i.e. do the most massive stars form throughout the star cluster, or only in its centre, or perhaps only in the densest clumps. It has already been shown that mass-segregated clumps form mass-segregated clusters (McMillan et al. 2007, Fellhauer et al. 2009). We can also address questions concerning 'field' OB stars.

The main question in this research is, does the introduction of an IMF help to erase the initial clumpy sub-structure faster, leading to a lower stochasticity of the results, or rather does it simply increase the randomness of the outcome?

The core ideology in this part of the project is to not only add one ingredient after the other to the models, but also to study their influence on the results separately, and then in pairs to deduce their interactions with each other. Only in this way it is possible to obtain a deep understanding of the different effects on the embedded clusters, as well as understanding their relative importance.

2 Star Clusters Dynamics

2.1 Dynamical Equilibrium in Collisional Systems

The virial ratio (Q), a usefull quantity to characterize a dynamical system, is defined as:

$$Q = \left| \frac{K_{\rm tot}}{W_{\rm tot}} \right| \tag{1}$$

that is, Q is the ratio between the total kinetic energy of the particles ($K_{\rm tot}$) and total gravitational potential energy of the system ($W_{\rm tot}$), which may include an external field. If we assume that a star cluster is in virial equilibrium $Q_{\rm eq}$ or virialized, it will be in a static, stable and unchanging configuration:

$$Q_{\rm eq} = 0.5 \tag{2}$$

In such virialized systems we could use the velocity dispersion of 'pressure' supported systems (σ) and the scale-length ($R_{\rm sc}$) to estimate the mass required to keep the system in a stable and unchanging configuration. We call this dynamically calculated mass 'dynamical mass' ($\rm M_{dyn}$); (Binney & Tremaine, 2008). Assuming that these systems follow a lowered isothermal distribution like a King profile we can use the following relationship (Illingworth, 1976):

$$M_{\rm dyn} = 167\, r_{\rm core}\, \sigma_0^2 \tag{3}$$

where $r_{\rm core}$ is the core radius of the King profile and σ_0 is the central velocity dispersion. A system in virial equilibrium is defined by a distribution function, which is independent of time. In some cases a small variation of the equilibrium may affect the system, for example a number of collisions may occur between the particles in the system, changing their orbits and leading to a change of the distribution function on long time-scales. This time-scale is the relaxation time scale, for which Binney & Tremaine (2008) derive an approximation:

$$t_{\rm relax} = \left(\frac{0.1\, N}{\ln N} \right)_{\rm n_{relax}} t_{\rm cross} \tag{4}$$

where N is the number of particles in the system, and $t_{\rm cross}$ is the crossing time, a characteristic time for a particle to cross the system, which may be approximated as $t_{\rm cross} \approx 2 * R/\sigma$ where R is the size of the system and σ is the velocity dispersion of the particles. We show below a list with typical values for several galactic and stellar systems:

1. Cluster of galaxies: $N = 10^3$, $t_{\rm cross} = 10^3$ Myr, $t_{\rm relax} \sim 10^4$ Myr
2. Galaxy: $N = 10^{11}$, $t_{\rm cross} = 10^2$ Myr, $t_{\rm relax} \sim 10^{10}$ Myr
3. Galactic nucleus: $N = 10^8$, $t_{\rm cross} = 0.01$ Myr, $t_{\rm relax} \sim 10^4$ Myr
4. Globular star cluster: $N = 10^5$, $t_{\rm cross} = 0.1$ Myr, $t_{\rm relax} \sim 10^2$ Myr

5. Open Cluster: $N = 10^2$, $t_{\rm cross} = 1$ Myr, $t_{\rm relax} \sim 10^1$ Myr

In the case of an embedded star cluster the assumption of virial equilibrium may not be true. Baumgardt and Kroupa (2007) performed simulations of star clusters under virial equilibrium, based on the argument that the time-scale of the formation of stars cluster is in the order of $\sim$1 Myr, which is a much longer time than the typical crossing time-scale of a star cluster. This would imply that at the moment of gas expulsion, the system would be already virialized.

We follow previous research done by Fellhauer et al. (2002) and Smith et al. (2012) simulating star clusters initially out of dynamical equilibrium. In Fig.4 we show the virial ratio (Q) as a function of time for recently formed star cluster (Smith et al., 2012). The virial ratio has strong oscillations, going from supervirial values or dynamical *hot* values $Q > 0.5$ to subvirial or dynamical *cold* values $Q < 0.5$. The amplitude of the oscillations decreases with time, showing the virialization of the system. Even though the stars may be completely out of equilibrium at the start of the simulation they violently relax and come close to virialization within 2-3 crossing-times - but they don't entirely dynamically relax. These simulations are made with equal mass particles and therefore there are some mechanisms that operate very weakly or do not exist, like mass-segregation. A particle system like a star cluster will always try to virialize due to the principle of energy equipartition (Spitzer, 1987).

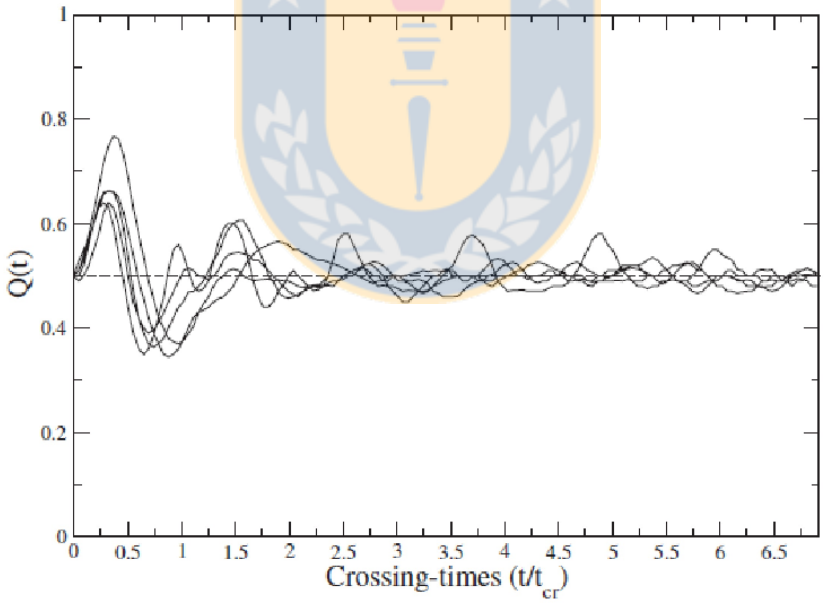

Figure 4: Plot of the virial ratio Q versus time (Smith et al., 2012). Each curve belongs to a different fractal distribution. All simulations here are made with equal mass particles. The initial virial ratio is 0.5, but due to the initial clumpy distribution it oscillates. With time the system tries to reach virial equilibrium (a constant 0.5) and the amplitude of the oscillations decreases.

Internal stellar encounters in star clusters transfer energy between the stars. Some stars may gain enough kinetic energy to get gravitationally unbound and escape from the cluster.

Given enough time a cluster could eject all its stars. Binney & Merrifield (1998) call this time the evaporation time ($t_{\rm ev}$). Lada & Lada (2003) make a rough estimation of $t_{\rm ev}$ for virialized open clusters:

$$t_{\rm ev} \approx 10^2\, t_{\rm vir} \tag{5}$$

2.2 Mass-Segregation

As explained in the introduction the stars in a cluster possess different masses, following a specific mass distribution law, the Initial Mass Function (IMF). Is has been observed in star clusters that the massive stars are preferentially distributed in the centre of the clusters, an effect that is called *mass-segregation*.

The mass-segregation could be primordial, i.e. from the moment of the formation of the stars within the molecular cloud (Chen et al. (2007),Weidner et al. (2010)). Another possibility is that the clusters achieve mass segregation through dynamical evolution. Particle systems like star clusters will always try to reach virial equilibrium and energy equipartition (Spitzer, 1987), and in star clusters stars have gravitational potential energy and kinetic energy. The fact that stars cannot change their masses, but can change their velocities and positions within the star cluster, will generate a spatial and kinematical segregation.

Allison et al. (2009) show that in star clusters like the Orion Nebula Cluster the mass-segregation for stars $M \geq 4M_{\odot}$ may occur quite fast. Spitzer (1969) find an analytical approximation for the time-scale that takes for a star of mass m to segregate $t_{\rm seg}$ or to 'sink' within a cluster:

$$t_{\rm seg}\,(m) \approx \frac{\langle M \rangle}{m} t_{\rm relax} \tag{6}$$

where $\langle M \rangle$ is the average mass of a star in the cluster and $t_{\rm relax}$ is given in Eq.4 (in fact the authors use a factor of (1/8) rather than 0.1), and therefore the equation may be rewritten as:

$$m \approx \frac{\langle M \rangle}{t_{\rm seg}} \frac{N}{8 \ln N} \frac{R}{\sigma} \tag{7}$$

Allison et al. (2009) analyse low mass clusters with $N = 300$-500 stars, $R \sim 0.1$-0.2 pc, $\langle M \rangle = 0.4$ M$_{\odot}$, and $\sigma = 2$ km s^{-1}. Dense cores with lifetimes of 0.1 Myr would allow mass segregation of stars above $M \sim 2$-4 M$_{\odot}$. Clumpy subvirial clusters are able to mass-segregate whilst smooth subvirial clusters cannot (Bonnell & Davies, 1998), because clumpy clusters are able to collapse to a much denser state than smooth clusters. The denser the medium ($\rho_{\rm med}$) where a massive star (m) is , the stronger the dynamical friction ($\vec{F}_{\rm fr}$) will be, as shown by the equation:

$$\vec{F}_{\rm fr} \sim -\rho_{\rm med} \frac{m}{\vec{v}^2} \hat{v} \tag{8}$$

where $\vec{v}$ is the velocity of the massive star. We notice that the sign of the force is negative and therefore the acceleration opposes to the velocity. As a consequence this force will slow down the massive stars and sink them to the centre of the cluster.

2.3 Cloud of Gas and Mass-Loss

When massive stars are formed in an embedded cluster, they dump large amounts of energy into the parent cloud, disrupting and finally expelling the gas of the system. This gas expulsion may determine the survival of a cluster, considering that the mass of the gas may constitude about $\sim$70% or more of the total mass of the cluster (Lada & Lada, 2003). The process of gas expulsion may occur between two extremes: a slow mass loss rate and a rapid mass loss rate. In a rough approximation we can obtain an analytical expresion for each regime (Stahler, 2012). We assume that the gas is a spherical cloud of ideal gas, where we write the total energy of the gas ($E_{\rm gas}$) as the sum of its kinetic energy ($1/2MV^2$), and its total gravitational energy ($-\eta G\frac{M^2}{R}$) as:

$$E_{\rm gas} = 1/2MV^2 - \eta G\frac{M^2}{R} \tag{9}$$

where V is the characteristic fluid velocity, M the mass of the gas, R the radius of a spherical distribution of gas, G is the gravitational constant and η is a pure number of order unity whose precise value depends on the cloud's density profile.

If the mass loss rate is slow, the virial equilibrium of the cloud is maintained with time, and the energy and the size of the cloud change in the form:

$$E_{\rm gas} = E_{\rm ini}\left(M/M_{\rm ini}\right)^3 \tag{10}$$

$$R = R_{\rm ini}\left(M_{\rm ini}/M\right) \tag{11}$$

where $M_{\rm ini}$ and $E_{\rm ini}$ are total initial mass and energy of the system. The equations show that as the total bound mass M decreases, the size of the cloud R increases in a hyperbolic form.

If the mass loss is fast enough that the size (R_o) and the characteristic fluid velocity (V_o) of the cloud remains constant, in the way:

$$E_{\rm gas} = 1/2MV_o^2 - \eta G\frac{M^2}{R_o} \tag{12}$$

Then the change of the total energy is (Stahler, 2012):

$$E_{\rm gas} = E_o\left(1-\Delta M/M_o\right)\left(1-2\Delta M/M_o\right) \tag{13}$$

Where M_o is the initial mass and ΔM is the expelled mass. This equation shows that if the mass loss is larger than double the initial mass ($\Delta M \geq M_0/2$), then the system changes to an unbound state. This simple approximation shows that if a gas cloud at the moment of gas expulsion (triggered by stellar evolution) does not convert half its mass into stars, and/or retain half its mass in form of gas, the whole system changes to an unbound state. Numerical simulations (Baumgardt and Kroupa, 2007) showed that the previous analytical estimate can be lowered to $\approx 70\%$ for fast gas-expulsion and as low as $\approx 80\%$ for slow gas-expulsion.

Although our models are an improvement and more realistic, with their clumpy initial distribution of stars, the remaining gas is distributed smoothly inside the cluster and does

not evolve with time. In reality, the gas is turbulent, and follows a filamentary structure of its own. Furthermore it is spatially and dynamically affected by stellar feedback processes. For example the UV-radiation of massive O-stars can ionize gas and alter the gas distribution. In low density regions, radiative feedback can be responsible for the expulsion of large quantities of the gas (Dale et al. 2012).

Another feedback mechanism is the mass-outflow from young stars. While the importance of proto-stellar jets in high-mass stars is still under debate (Guzman et al., 2012), the outflow of solar winds from intermediate mass stars will have an influence on the gas distribution, and may even be able to expel the gas completely from an embedded cluster (e.g. Weidner et al. 2007 and references therein).

2.4 Star Formation Efficiency and the Local Stellar Fraction

Stars form in embedded clusters within the dense cores of Giant Molecular Clouds GMCs. The star formation efficiency (SFE) is an indicator of the amount of mass in gas converted into stars, quantified as the fraction of the mass in stars and the total mass of the system. It is defined by (Lada & Lada, 2003) as:

$$\mathrm{SFE} = \frac{M_{\mathrm{tot}}^{\mathrm{stars}}}{M_{\mathrm{tot}}^{\mathrm{stars}} + M_{\mathrm{tot}}^{\mathrm{gas}}} \tag{14}$$

where $M_{\mathrm{tot}}^{\mathrm{stars}}$ is the mass in stars while they are still embedded in the gas cloud. $M_{\mathrm{tot}}^{\mathrm{gas}}$ is the mass of the gas not converted into stars.

Baumgardt and Kroupa (2007) performed several numerical simulations to predict the survival of star clusters to the expulsion of the gas. They compare the SFE with the remaining gravitationally bound mass of the cluster ($M_{\mathrm{f}}^{\mathrm{stars}}$) after the gas-expulsion, which is quantified as the bound fraction f_{bound}:

$$f_{\mathrm{bound}} = \frac{M_{\mathrm{f}}^{\mathrm{stars}}}{M_{\mathrm{tot}}^{\mathrm{stars}}} \tag{15}$$

In their experiments they use slow and rapid mass-loss rates and the assumption of a system in virial equilibrium at the moment of gas-expulsion. Smith et al. (2012) performed similar simulations, but with a system initially out of equilibrium. In Fig. 5 we show the results of Smith et al. (2012) and Baumgardt and Kroupa (2007) for comparison. We see that the simulations initially in equilibrium predict no survivors for SFEs of 20 %. On the other hand, using systems out of equilibrium, it was possible to obtain survivors using a SFE of 20%.

To better explain the state of a star cluster at the moment of gas-expulsion, Smith et al. (2012) replace the SFE with the Local Stellar Fraction (LSF), defined as:

$$\mathrm{LSF} = \frac{M^{\mathrm{stars}}\left(r < r_{\mathrm{h}}^{\mathrm{stars}}\right)}{M^{\mathrm{stars}}\left(r < r_{\mathrm{h}}^{\mathrm{stars}}\right) + M^{\mathrm{gas}}\left(r < r_{\mathrm{h}}^{\mathrm{stars}}\right)} \tag{16}$$

where $M^{\mathrm{stars}}(r_{\mathrm{h}})$ is the mass of the stars, $M^{\mathrm{gas}}(r_{\mathrm{h}})$ the mass of the gas, both calculated within the half mass radius of the stars ($r_{\mathrm{h}}^{\mathrm{stars}}$).

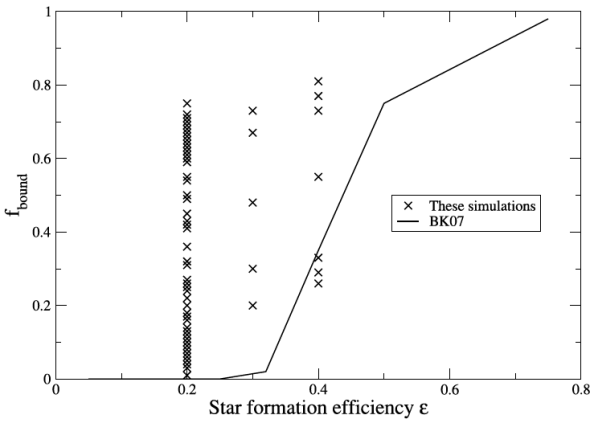

Figure 5: Plot of results from Smith et al. (2012) for the final bound fraction $f_{\rm bound}$ versus the Star Formation Efficiency SFE (marked with crosses), compared with the results of Baumgardt and Kroupa (2007) (line). Several surviving clusters were obtained in simulations using a SFE of 20% while under the assumption of virial equilibrium this could not be possible.

While the SFE is constant throughout time for each simulation, the LSF evolves with time. The initially out off equilibrium cluster contracts and expands with time, changing its concentration and therefore also the half mass radius. The mass of the gas is calculated within the same half mass radius causing the changes in the LSF. In the next section we show that Smith et al. (2012) use the LSF at the moment of the expulsion of the gas to predict the final bound mass of the cluster.

2.5 Equal Mass Particle Simulations

Using systems out of virial equilibrium it was possible to obtain surviving clusters with a SFE $= 20\%$. Furthermore, the simulations made by Smith et al. (2012) and Farias et al. (in prep.) for equal mass stars leads to a relation or trend between the Local Stellar Fraction and the final bound fraction when $Q_{\rm f} = 0.5$. This relation reads:

$$f_{\rm bound} \quad = \quad ({\rm LSF} - \omega)^{\alpha} \tag{17}$$

where ω denotes the offset of LSF when the bound fraction is zero. Fitting all their data, which considered Uniform and Plummer gas distributions for the cloud, different initial virial ratios $Q_{\rm i}$ and different initial fractal distributions, they found values of $\omega = 0.176 \pm 0.002$ and $\alpha = 0.47 \pm 0.01$. In Fig.6 we show the data marked with crosses, together with the trend marked with the red curve. Over-plotted are the binned mean values, which are calculated with the same number of data points.

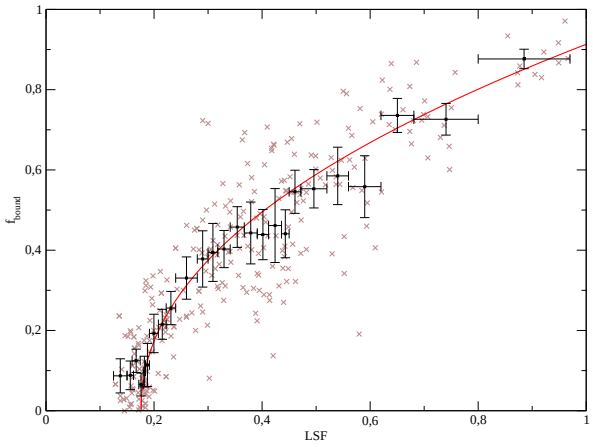

Figure 6: Taken from Farias et al. (in prep.); the bound fraction measured at 15 Myr ($f_{\rm bound}$) versus the Local Stellar Fraction (LSF). The simulations here use equal mass stars with different initial fractal distributions and different initial virial ratios $Q_{\rm i}$. Over-plotted are the binned mean values, which are calculated with the same number of data points. The red curve denotes the fit of Eq.17. The parameters of the fit are $\omega = 0.176 \pm 0.002$ and $\alpha = 0.47 \pm 0.01$.

2.6 The Initial Mass Function

As we already mentioned, all previous simulations were made using the same mass for each star to simplify the models and to study each variable independently. Of course reality is more complicated. According to observations stars form in groups from a single Giant Molecular Cloud where each star has a different mass. Observations also show that the spectrum of masses in these groups of stars follow an apparently universal distribution. We have no *a priori* reason to suppose that this distribution is universally applied to all observed starbursts that occurred under remarkable different circumstances over the entire age of the Galaxy (Binney & Merrifield "Galactic Astronomy" 1998) although until now observations indicate that this could be the case (Kroupa, 2001). Also recent simulations show hints of how different mechanisms such as radiative feedback (Bate, 2009) could help in shaping an universal law. This distribution function, called the 'Initial Mass Function' (IMF) shows that in a recently formed cluster we usually find a high number of low mass stars and a low number of high mass stars. Then according to stellar evolution theory, the high mass stars get destroyed through supernova events. This induces the expulsion of the gas, which will ultimately destroy the GMC and trigger the escape of some, if not all, the stars from the cluster. The IMF can be inferred from the luminosity function $\Phi(L)$ using the stellar mass-luminosity $m(L)$ relation together with a model of how the star formation rate varies with time (Binney & Merrifield, 1998). The IMF gives the number of stars present within a mass range: $(m, m + dm)$.

$$\frac{dN}{dm} = \xi(m) \tag{18}$$

In general the IMF is a power-law of the form:

$$\xi(m) \quad \propto \quad km^{-\alpha} \tag{19}$$

k is a normalizing constant which is given by choosing the total stellar mass of the cluster $M_{\rm tot}^{\rm stars}$ (embedded cluster). $M_{\rm tot}^{\rm stars}$ is the mass in stars prior to gas expulsion, thus prior to any losses of the stellar population due to cluster expansion (Kroupa & Boily 2002):

$$M_{\rm tot}^{\rm stars} \quad = \quad \int_{m_{\rm min}}^{m_{\rm max}} m\xi(m)dm \tag{20}$$

2.6.1 The Salpeter-IMF and the Scalo-IMF

Salpeter (1955) proposed with the then-available data an IMF of the form:

$$\xi\left(m\right) \quad \propto \quad m^{-2.35} \tag{21}$$

i.e. $\alpha = 2.35$. It shows that the number of stars in each mass range decreases rapidly with increasing mass, as shown in Fig. 7. But this IMF is suitable only for a limited range of stellar masses, around values of $0.5\,{\rm M}_\odot < m < 1\,{\rm M}_\odot$. To better represent the whole mass-spectrum of stellar masses in a cluster, J. Scalo (1986) introduced a logarithmic normal distribution. This distribution may be fitted by a broken power law IMF (Binney & Merrifield, 1998), that has different power coefficients α for different stellar mass ranges:

$$\xi(m) \propto \begin{cases} m^{-1.83} & \text{for } \; m < 0.2{\rm M}_\odot \\ m^{-3.27} & \text{for } \; 1{\rm M}_\odot < m < 10{\rm M}_\odot \\ m^{-2.45} & \text{for } \; 10{\rm M}_\odot < m \end{cases} \tag{22}$$

2.6.2 The Kroupa-IMF

Kroupa (2001) introduced a fourth component power-law with different αs for the different stellar mass ranges in a star cluster:

$$\xi(m) \propto \begin{cases} m^{-0.30} & \text{for } \; 0.01{\rm M}_\odot \leq m \leq 0.08{\rm M}_\odot \\ m^{-1.30} & \text{for } \; 0.08{\rm M}_\odot \leq m \leq 0.5{\rm M}_\odot \\ m^{-2.30} & \text{for } \; 0.5{\rm M}_\odot \leq m \leq 1{\rm M}_\odot \\ m^{-2.35} & \text{for } \; 1{\rm M}_\odot \leq m \end{cases} \tag{23}$$

where at the low mass end the regime from super Jupiters and brown dwarves $0.01\ {\rm M}_\odot \leq m \leq 0.08\ {\rm M}_\odot$ to the low mass stars is added.

2.6.3 The Maximum Stellar Mass & The Modified Kroupa-IMF

The IMF gives the numbers of stars within a mass range $(m; m+dm)$. Equation 20 can relate and constrain the maximum mass of the stars $m_{\rm max}$, with the total mass of the system $M_{\rm tot}^{\rm stars}$, in the way $m_{\rm max} = m_{\rm max}\,(M_{\rm tot}^{\rm stars})$. The more massive the cluster is, the more massive the most massive star would be, reaching values more massive than what has been observed or predicted by theory. To solve this issue Weidner and Kroupa (2004) introduced restrictions in the IMF to limit the mass of stars to a maximum of 150 $\rm M_\odot$. For that the authors introduced the following IMF:

$$\xi(m) \propto \begin{cases} \left(\frac{m}{m_H}\right)^{-\alpha_0} & \text{for } m_{\rm low} \leq m \leq m_{\rm H} \\ \left(\frac{m}{m_H}\right)^{-\alpha_1} & \text{for } m_{\rm H} \leq m \leq m_0 \\ \left(\frac{m_0}{m_H}\right)^{-\alpha_1} \left(\frac{m}{m_0}\right)^{-\alpha_2} & \text{for } m_0 \leq m \leq m_1 \\ \left(\frac{m_0}{m_H}\right)^{-\alpha_1} \left(\frac{m_1}{m_0}\right)^{-\alpha_2} \left(\frac{m}{m_1}\right)^{-\alpha_3} & \text{for } m_1 \leq m \leq m_{\rm max} \end{cases} \tag{24}$$

$$\begin{cases} \alpha_0 = 0.30 & \text{for } 0.01{\rm M_\odot} \leq m \leq 0.08{\rm M_\odot} \\ \alpha_1 = 1.30 & \text{for } 0.08{\rm M_\odot} \leq m \leq 0.5{\rm M_\odot} \\ \alpha_2 = 2.30 & \text{for } 0.5{\rm M_\odot} \leq m \leq 1{\rm M_\odot} \\ \alpha_3 = 2.35 & \text{for } {\rm M_\odot} \leq m \end{cases} \tag{25}$$

In Fig. 7 the new constrained IMF is compared with an unconstrained IMF. At high stellar masses the new IMF gives less stars than the unconstrained IMF and forbid stars with more massive than $150\,M_\odot$.

As we mentioned before, there should be a relation between the total mass of a cluster, and the maximum mass of its stars, $m_{\rm max} = m_{\rm max}\,(M_{\rm tot}^{\rm stars})$. Weidner et al. (2007) find a numerical solution to Eq.20 using the Kroupa-IMF, shown in Fig.8. The unconstrained IMF ($m_{\rm max} = \infty$) shows that the more massive a star cluster is ($\rm M_{tot}^{stars}$), the more massive the most massive stars are, reaching unphysical values. The value to constrain the IMF reaches a maximum of 150 $\rm M_\odot$ no matter how massive the cluster is. We see this in Fig. 8 where for values of $\rm M_{tot}^{stars}$ higher than $10^{2.5}$ $\rm M_\odot$, the values of $m_{\rm max}$ are different depending on the IMF used.

We use star clusters with a fixed initial total mass of $M_{\rm tot}^{\rm stars} = 500$ $\rm M_\odot$. This gives us a maximum stellar mass of about $m_{\rm max} \sim 10^{1.4}$ $\rm M_\odot \sim 25$ $\rm M_\odot$.

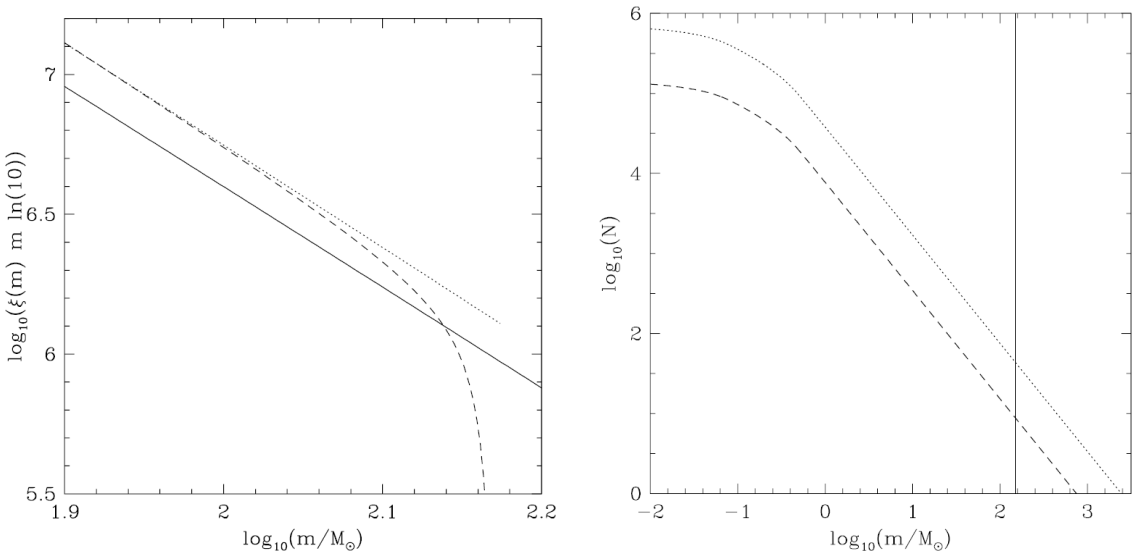

Figure 7: Taken from Weidner & Kroupa 2003. *Left:* The "logarithmic" IMF ($\xi_L(m) = \xi(m) m \ln 10$) over logarithmic stellar mass above 80 $M_\odot$ for three different cases. The solid line shows an unlimited Salpeter IMF, the dotted line a Salpeter IMF truncated at $m_{\max *} = 150\ M_\odot$ and the dashed line show the IMF restricted by the author's method. All three cases are normalized to the same area over $0.01 \leq m/M_\odot \leq \infty$. *Right:* Number of stars (logarithmic) above mass m for different total masses, dotted line: $M = 2.5 \times 10^5\ M_\odot$; dashed line: $M = 5 \times 10^4\ M_\odot$, Selman et al 1999). The vertical line marks $m = 150\ M_\odot$.

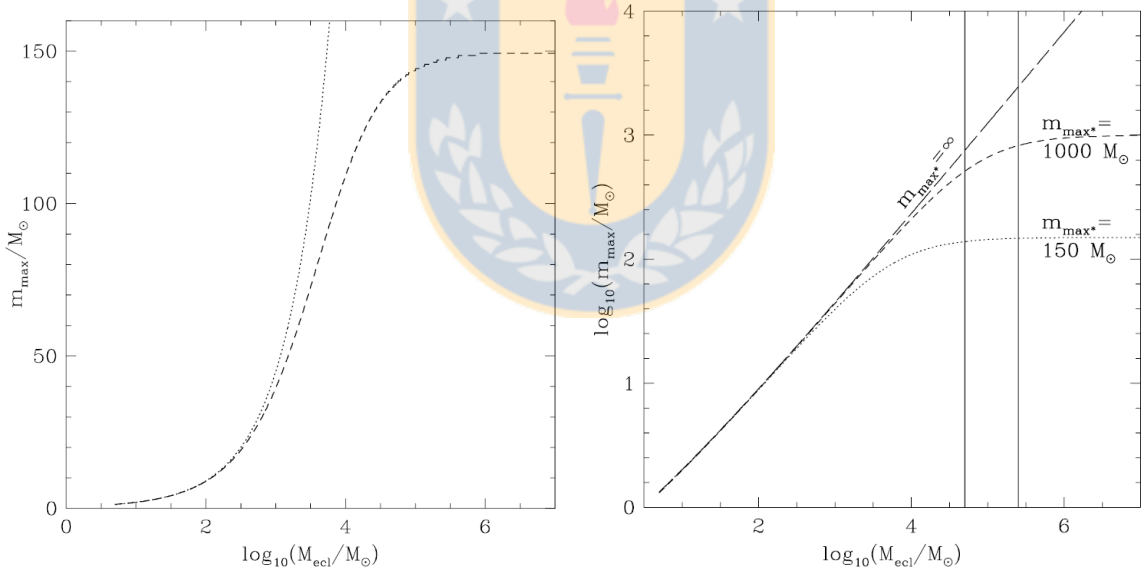

Figure 8: Taken from Weidner & Kroupa 2003. *Left:* Dependence of the stellar upper mass limit, $m_{\max}$, on the cluster mass for a limited ($m_{\max *} = 150\ M_\odot$) and the unlimited fundamental upper stellar mass and $\alpha = 2.35$. *Right:* Double logarithmic plot of the maximal stellar mass versus the cluster mass. Three cases are shown: finite upper mass limit of $m_{\max *} = 150\ M_\odot$ (dotted line); $m_{\max *} = 1000\ M_\odot$ (short-dashed line); and no limit $m_{\max *} = \infty\ M_\odot$ (long-dashed line). The vertical lines mark the empirical mass interval for the cluster R136 in the LMC.

3 The Codes

3.1 NBODY 6

Our simulations are performed with NBODY 6, developed by S. Aarseth (see Aarseth 2003 for a full description of the code). This code is a direct N-body code that solves many-body systems like a star cluster with high precision. It has special regularization routines to handle close encounters between two and more stars and a special treatment for binary stars, to allow fast computations without losing resolution or accuracy.

The code has in-built routines for an analytical background potential with which we are able to mimic the gas component. It also allows us to remove this background potential instantaneously or as a smooth function of time at a certain pre-defined instant (the time of gas-expulsion). We are therefore able to model the gas-expulsion of the embedded cluster at different starting times and with different durations.

NBODY 6 allows stars to have different masses according to an initial mass function (IMF). In our project we will use the standard Kroupa-IMF (Kroupa et al. 1990 and follow-up publications). To assign masses according to this IMF, NBODY 6 has a built-in routine. Nonetheless we build and use our own IMF-generator.

3.2 IMF Generator

We use the Kroupa IMF in Eq.24 and Eq.25 to generate different samples of masses for the stars. As we are interested only in the stellar component, we do not uses the substellar mass range (below 0.08 $M_\odot$ for brown dwarfs). Using a total stellar mass of 500 $M_\odot$, gives us an analytical value of 892 stars. To generate different samples we develop a code that use the Inverse Cumulative Distribution Function (ICDF) method : first the equations are analytically integrated, and second we use a Monte Carlo method to generate random mass samples, from which the IMF distribution is selected. We force the total stellar mass to be 500 $M_\odot$, obtaining variations of less than 0.16%, and the number of stars varies from 705 to 1064, with an average of 920 stars. In Fig.9 we show one of our mass samples: it has 901 stars and we can see that for the range of the more massive stars ($M \geq 1\ M_\odot$) the power law has a coefficient of $\alpha_3 \sim 1.91$, lower than the model ($\alpha_3 = 2.35$). Kroupa (2001) explain that this variation is due to the low number statistics, and this value would be within the expected range as the authors show (see Fig.3 of Kroupa (2001)).

3.3 Fractal Generator

We use the code developed by Goodwin & Whitworth (2004) which uses a box fractal method to generate a fractal-shape distribution of stars (see. Fig.10), defining an *ur*-cube with side 2, and placing an *ur*-parent at the centre of the *ur*-cube. Then the *ur*-cube is divided into $N_{\rm div}^3$ equal subcubes, and a child is placed at the centre of each sub-cube (the first generation). Usually $N_{\rm div} = 2$ is used, which gives 8 sub-cubes and 8 first-generation children. The probability that a child matures to become a parent in its own right is $N_{\rm div}^{D3}$, where

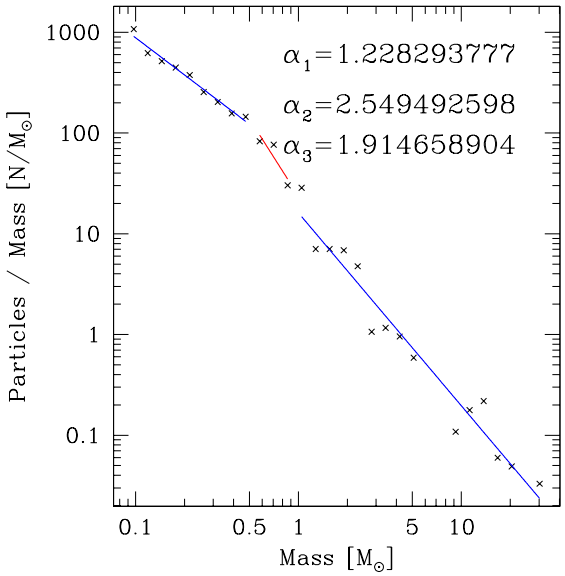

Figure 9: We show one of our mass samples. This has 901 stars and we may see that for the range of the massive stars the slope is $\alpha_3 \sim 1.91$, lower than the model ($\alpha_3 = 2.35$). This is due to low number statistics, as explain by Kroupa (2001).

D is the fractal dimension; for lower D, the probability that a child matures to become a parent is lower. Children that do not mature are deleted, along with the *ur*-parent. A little noise is then added to the positions of the remaining children, to avoid an obviously gridded structure, and they become the parents of the next generation, each one spawning $N_{\rm div}^3$ children (the second generation) at the centres of $N_{\rm div}^3$ equal-volume sub-sub-cubes, and each second generation child having a probability $N_{\rm div}^{D-3}$ of maturing to become a parent. This process is repeated recursively until there is a sufficiently large generation that, even after pruning to impose a spherical envelope of radius 1 within the *ur*-cube, there are more children than the required number of stars. Children are then culled randomly until the required number is left, and the surviving children are identified with the stars of the cluster. For our simulations we choose a fractal dimension $D = 1.6$.

3.4 Snow Ball Method

We use the code developed by Farias et al. (in prep.) to measure the fraction of the mass in a cluster that is gravitationally bound using an energy criterion. If the star cluster is not destroyed after the gas expulsion, we have to identify the number of star cluster's sub clumps and select the most massive one. The code begins to analyse the particles around the main sub clump, progressively increasing the volume around the clump (as a snowball) and calculate the bound material until it covers the whole region. This is done for a specific frame of time, as in each time-step or frame the bound/unbound particles may change. A more detailed description of this method can be found in Farias et al. (in prep.).

4 Setup of the Simulations

Our main goal is to analyse how the introduction of the Initial Mass Function changes the trend found for the survival of embedded clusters to gas expulsion $f_{\rm bound}^{15\,{\rm Myr}}\,({\rm LSF},\,Q_{\rm f})$. For that the first task is to generate different samples of stars with different masses that follow the Kroupa IMF. Then we also generate fractal spatial-distributions of stars with virial and sub-viral initial conditions. We set a cloud of gas around the stars modeled with an analytical potential. The mass in stars and in gas is set to such that SFE $= 20\%$. We then start the simulation of the cluster embedded in the gas until the moment of gas-expulsion $t_{\rm exp}$, when the gas is expelled with a rapid mass-loss rate. The simulation continuous without gas and stops at 15 Myr when we measure the remaining mass of the cluster.

4.1 Paramater Space: Seven Cases

Our parameter search is organized around seven cases:

A: We use one sample of masses of the stars or 'IMF-sample', one fractal distribution for the positions of the stars and a Plummer gas distribution. We still have one degree of freedom: where we position each mass of the IMF-sample within the fractal distribution. We use a random positioning to explore a broad paramater space and we call this a 'random initial positioning (RIP)'. We choose a fixed gas-expulsion time $t_{\rm exp} = 5$ Myr and two initial virial ratios: $Q_{\rm i} = 0.2$ and $Q_{\rm i} = 0.5$. We then measure the bound fraction of the remaining star cluster at 15 Myr ($f_{\rm bound}^{\rm 15Myr}$).

B: Similar to case A, but we fix the initial virial ratio to $Q_{\rm i} = 0.2$ and we choose two expulsion times: $t_{\rm exp} = 3.85$ Myr and $t_{\rm exp} = 5.00$ Myr, and measure the bound fraction at 15 Myr $f_{\rm bound}^{\rm 15Myr}$.

C: We use a fixed gas potential and an expulsion time of $t_{\rm exp} = 5$ Myr. We use only one IMF-sample for all the simulations. We use different fractals for the spatial distribution with random initial positioning RIP. We also use two initial virial ratios: $Q_{\rm i} = 0.2$ and $Q_{\rm i} = 0.5$ and measure the bound fraction at 15 Myr $f_{\rm bound}^{\rm 15Myr}$.

D: In this case we use one fixed IMF-sample and one fixed fractal distribution. We use two initial virial ratios, $Q_{\rm i} = 0.5$ and $Q_{\rm i} = 0.0$ and measure the bound fraction at 15 Myr $f_{\rm bound}^{\rm 15Myr}$. For comparison we perform one simulation with the same fractal, but with equal mass particles. We fix the final virial ratio to be $Q_{\rm f} = 0.5$, giving us a range of expulsion times between $t_{\rm exp} = 1.2$ Myr and $t_{\rm exp} = 3.08$ Myr. We use two gas potentials: a Plummer potential and a Uniform sphere.

E: We use different mass samples with different fractal distributions with random initial spatial distributions for the masses (stars), using two initial virial ratios: $Q_{\rm i} = 0.0$ and $Q_{\rm i} = 0.5$. We use the same set of fractals with equal mass particles to compare the variations with the IMF simulations. And as in the previous case, we use expulsion times $t_{\rm exp}$ set by fixing $Q_{\rm f} = 0.5$. We measure the bound fraction at 15 Myr f_{bound}^{15Myr}.

F: Here we use the set for the simulations of case D, but we also measure the bound fraction at 2.97 Myr ($f_{\rm bound}^{2.97{\rm Myr}}$).

G: Similar to case E. We use different IMF samples for the stars, with different fractal distributions. Instead of a random initial spatial distributions for the masses (stars), we use a primordial or initial mass segregation. We also using two initial virial ratios: $Q_{\rm i} = 0.0$ and $Q_{\rm i} = 0.5$. We use the same set of fractals with equal mass particles to compare the variations with the IMF simulations. And as in the previous case E, we use expulsion times $t_{\rm exp}$ set by fixing $Q_{\rm f} = 0.5$. We measure the bound fraction at ~ 4.5 and 15 Myr.

Table 1 summarizes the parameters which fixed, or are allowed to vary, for each case above.

Table 1: Here are show which main parameters are changed (Var) or kept fixed (Fix) for the different cases. The column 'Gas' tells us if we choose two or one of the gas distributions. $Q_{\rm i}$, $Q_{\rm f}$, and $t_{\rm exp}$ show if we keep these quantities fixed or not. A Fix for $f_{\rm bound}$ indicates that we measured it always at the same time, and Var indicate that we measure it at different times.

Case	Gas	Fractal	Sample	$Q_{\rm i}$	$Q_{\rm f}$	$t_{\rm exp}$	$f_{\rm bound}$
A	Fix	Fix	Fix	Var	Var	Fix	Fix
B	Fix	Fix	Fix	Fix	Var	Var	Fix
C	Fix	Var	Fix	Var	Var	Fix	Fix
D	Var	Fix	Fix	Var	Fix	Var	Fix
E	Var	Var	Var	Var	Fix	Var	Fix
F	Fix	Fix	Fix	Var	Fix	Var	Var
G	Fix	Var	Var	Var	Fix	Var	Var

4.2 Total Stellar Mass

We use star clusters with a fixed initial total mass of $M_{\rm tot}^{\rm stars} = 500$ M$_\odot$. This gives us a maximum stellar mass of about $m_{\rm max} \sim 10^{1.4}$ M$_\odot$ ~ 25 M$_\odot$. We generate samples of masses with the only constraint that the stars cannot have masses higher than the maximum physical stellar mass, $m_{\rm max} = 150$ M$_\odot$. We are working with an idealized model and we want to explore a bigger parameter space that would be possible by choosing the maximum mass contrained by the total mass of the cluster (~ 25 M$_\odot$). Simulations including this constraint will be explored in future projects.

4.3 Fractal Distribution and Initial Virial Ratio

To mimic the filamentary structure observed or simulated (Bate, 2009) in the region of a forming star clusters we use a fractal distribution. We use the code developed by Goodwin &

Whitworth (2004), explained in Sec.3. In Fig. 10 we show the stars with a fractal distribution of one of our simulations. The black dots are particles with a mass range of 0.08 $M_\odot$ to 1 $M_\odot$, and the pink particles show masses within 1 $M_\odot$ and 30 $M_\odot$.

Star clusters do not necessarily have a fractal distribution, the range of scales over which young star clusters exhibit substructure is usually very small, often less than an order of magnitude, so the notion of a fractal cannot be applied rigorously. Nonetheless, fractals provide a simple, one-parameter description of clumpiness, and this is why we use them.

Figure 10: We show the stars in a fractal distribution of one of our simulations. The black particles are stars with a mass range of 0.08 $M_\odot$ to 1 $M_\odot$, and the pink particles show stars with masses between 1 $M_\odot$ and 30 $M_\odot$.

4.4 Gas Distribution and Mass loss Rate

To model the cloud of gas we use two sets of mass distributions, a Plummer profile and a uniform sphere. For both profiles we adjust their concentration to have a mass of gas of 2000 $M_\odot$ within the volume occupied by the stars ($R_{\rm max} = 1.5$ pc). The total mass of the stars is $500\ M_\odot$ resulting in a constant SFE of 20 %.

4.4.1 Gas Distribution: Set (i)

The Plummer density profile is given by:

$$\rho_{\rm Pl} = \frac{3M_{\rm Pl}}{4\pi r_{\rm Pl}} \tag{26}$$

$$\rho\left(r\right) = \rho_{\rm Pl}\left(1+\frac{r^2}{r_{\rm Pl}^2}\right)^{-5/2} \tag{27}$$

$$M\left(r\right) = M_{\rm Pl}\frac{r^3}{r_{\rm Pl}^3}\left(1+\frac{r^2}{r_{\rm Pl}^2}\right)^{-3/2} \tag{28}$$

where we use a Plummer radius of $R_{\rm Pl} = 2$ pc and the Plummer mass $M_{\rm Pl} = 9259.26$ $\mathrm{M}_{\odot}$.

4.4.2 Gas Distribution: Set (ii)

The uniform sphere of gas is given by a constant density profile:

$$\rho_o = \frac{M_{\rm tot}}{4\pi/3 r_{\rm c}^3} \tag{29}$$

$$\rho\left(r\right) = \rho_o \tag{30}$$

$$M\left(r\right) = \frac{M_{\rm tot}}{r_{\rm c}^3}r^3 \tag{31}$$

where we use a cutoff-radius $r_{\rm c} = 1.8$ pc and a total mass $M_{\rm tot} = 3472$ $\mathrm{M}_{\odot}$.

4.4.3 Mass-Loss Rate

In a slow mass-loss gas-expulsion process, clusters survive better than in the rapid mass loss case. In our scenarios we are working with the rapid mass loss rate used by Smith et al. (2012), modeled in the following form:

$$M_{\rm gas}\left(t\right) = \frac{M_{\rm init}}{1+\dot{M}\left(t-t_{\rm exp}\right)} \tag{32}$$

where the rate at which the gas is removed is set to$\dot{M} = 140$ Myr^{-1}

5 Results and Discussion

We performed more than 300 simulations with our models in order to explore and understand the relation between the properties of embedded clusters at the moment of gas expulsion and the final surviving star cluster. We start by analysing the main properties of our IMF samples. Then we explain in more detail one of our simulations with a representative example. Finally we organize our parameter search in different cases: A, B, C, D, E, F and G.

5.1 IMF Samples

We generate in total 12 IMF samples. Their total mass varies by less than 0.16%. The largest differences is visible in the number of stars, the amount of high mass stars and the mass of those massive stars. The sample with the lowest number of stars has 705 stars and the most massive star has 64.6 $M_\odot$. The sample with the most stars has 1064 stars, where the most massive star has only 13.8 $M_\odot$. This is the lowest massive star from the whole samples. Samples with a high number of stars tend to have less massive stars or very few very massive ones.

Table 2: Main properties of the samples of the IMF. First column designates the name of the sample. The second indicate the total number of star in each sample. The third column indicate the total stellar mass of each sample. Then the fourth column is the average mass for a star in each sample. The fifth is the most massive star of each sample. From the sixth to the eight column we give the number of stars for each interval of mass, which is as follow: $N^{\rm stars}_{\geq 16}$ is the number of stars with masses $m \geq 16$ $M_\odot$, then $N^{\rm stars}_{16-10}$ indicates the number of stars with masses between $16 > m/M_\odot \geq 10$ and finally $N^{\rm stars}_{10-2.1}$ is the number of stars in the range $10 > m/M_\odot \geq 2.1$.

$\mathrm{IMF}_{\rm sample}$	$N^{\rm stars}_{\rm tot}$	$M^{\rm stars}_{\rm tot}$	$\langle M_{\rm star}\rangle$	$m_{\rm max}$	$N^{\rm stars}_{\geq 16}$	$N^{\rm stars}_{16-10}$	$N^{\rm stars}_{10-2.1}$
n^o	n^o	[$M_\odot$]	[$M_\odot$]	[$M_\odot$]	n^o	n^o	n^o
1	901	500.24	0.56	30.3	2	6	21
2	891	500.11	0.56	30.5	3	0	32
3	948	500.06	0.53	27.2	1	2	33
4	906	500.31	0.55	20.7	1	1	37
5	972	500.32	0.52	29.3	1	0	37
6	816	500.03	0.61	61.3	2	4	26
7	1010	500.74	0.50	36.6	1	1	30
8	1064	500.31	0.47	13.8	0	4	27
9	1005	500.40	0.50	16.9	1	2	31
10	705	500.42	0.71	64.6	2	6	20
11	789	500.01	0.63	87.1	2	2	26
12	1018	500.80	0.49	30.8	3	0	23
$\langle mean\rangle$	919±32	500.31±0.08	0.55±0.02	37.4±6.65			

And samples with a low number of stars will tend to have more massive stars. This trend naturally comes from random sampling of a distribution function of the kind we are using. The most massive star among the samples has 87.1 $M_\odot$ and the parent distribution has 789 stars. In Table 2 we show the main properties of the samples used.

5.2 Representative Example

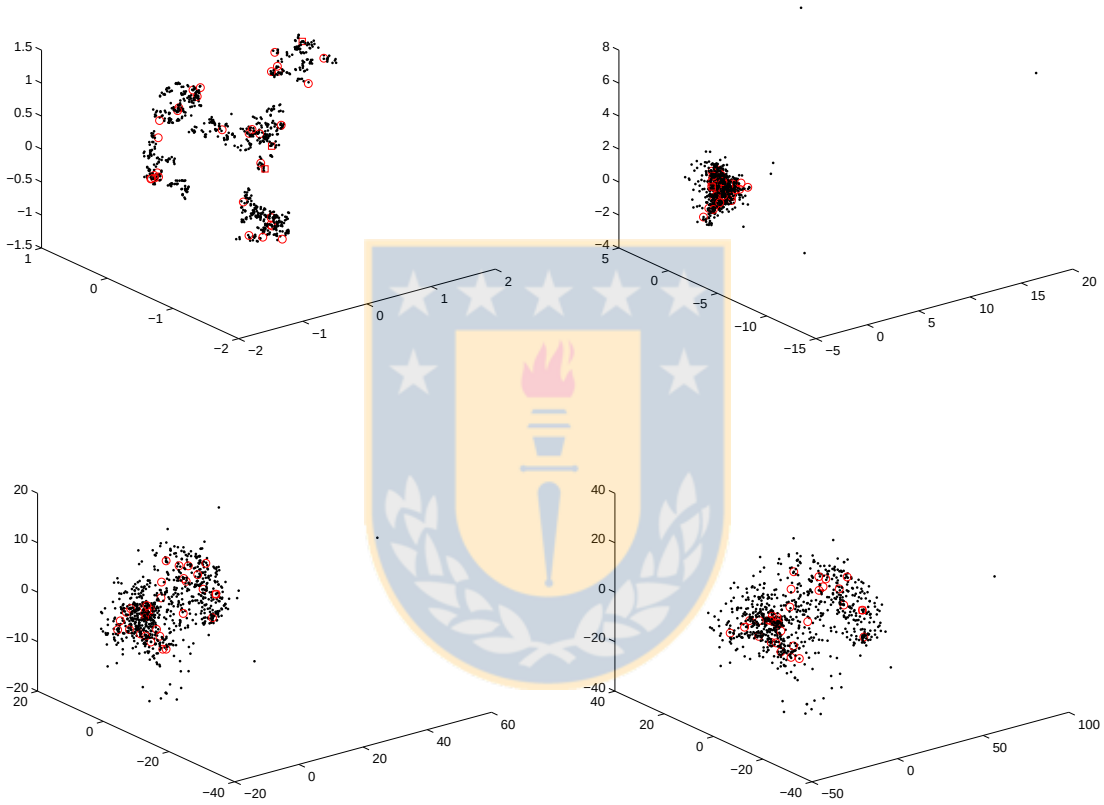

Figure 11: 3D snapshots of a representative example of our simulations. The axes show the extension in pc. Please note that the scales are different in each snapshot. The sample of stars correspond to $\mathrm{IMF}_{\mathrm{sample}} = 2$. Black points indicate the position of stars with masses between $0.08 < m/\mathrm{M}_\odot < 2.1$. The red circles are stars with masses between $2.1 < m/\mathrm{M}_\odot < 10$ and the red squares are the stars between $16 < m/\mathrm{M}_\odot < 50$ (this sample has no stars between $10 < m/\mathrm{M}_\odot < 16$). *Upper-left:* snapshot at $t = 0$ Myr showing the initial fractal distribution. *Upper-right:* snapshot at the moment of gas expulsion, $t = 5$ Myr, when the LSF is measured. The cluster collapsed to a more concentrated structure, having a LSF$=$ 0.29. Mass-segregation is already visible at this time-slice. *Bottom-left:* snapshot at $t =$ 10 Myr showing an expanded cluster on a larger scale ($\sim$ 20 pc). *Bottom-right:* snapshot at $t = 15$ Myr, when the bound fraction is measured; in this simulation we measured $f_{\mathrm{bound}}^{15Myr} =$ 0.14.

In this Section we explain how the models for our star clusters evolve with time. We choose one of our simulations as a representative example, i.e. Sim064. In Fig. 11 we show snapshots of the simulation. This simulation used the sample of masses $\mathrm{IMF_{sample}} = 2$. The initial virial ratio of the system is $Q_{\rm i} = 0.5$. We proceed by explaining each snapshot or panel in Fig. 11:

Snapshot 1 *Top-left panel:* taken at $t = 0$ Myr. We see that the stars are positioned in an initially fractal distribution with dimension 1.6, inside a radius of 1.5 pc. The masses of the stars follow a Kroupa-IMF, the $\mathrm{IMF_{sample}}$ n^o 2 of Tab.2. We assign the masses randomly to the stars within the fractal distribution, and therefore the cluster is not initially mass-segregated. The massive stars (red squares and circles) are scattered throughout the fractal. The stars are also initially embedded in a smooth cloud of gas modeled as a Uniform Sphere, i.e. uniform density sphere which contains 2000 $\mathrm{M_\odot}$ within 1.5 pc. This simulation has $Q_{\rm i} = 0.5$, i.e. the stars have velocities according to virial equilibrium but as they do not form a smooth equilibrium distribution their actual state is not virialized.

Snapshot 2 *Top-right panel:* taken $t = 5$ Myr. We show the state of the cluster just at the moment before the expulsion of the gas ($t_{\rm exp} = 5$ Myr). We see that the stars are more concentrated and show mass-segregation; a result from the collapse of the cluster from the initial out of virial equilibrium state. At this moment we measure the LSF, obtaining a value of $\mathrm{LSF} = 0.29$ in this simulation.

Snapshot 3 *Bottom-left panel:* taken at $t = 10$ Myr, showing the cluster after gas-expulsion. The mass-loss leaves several stars gravitationally unbound due to the violent relaxation induced by the gas-expulsion. These unbound stars escape away from the system. If we note the scale of the axis that is $\sim 20\,pc$, we may appreciate that the cluster is expanding.

Snapshot 4 *Bottom-right panel:* taken at $t = 15$ Myr. We see that the cluster continues to expand (with a scale now $\sim$ 30-50 pc), losing even more stars. This *evaporation* is due to internal mechanisms such as three body encounters, i.e. the cluster never reaches complete virial equilibrium. At this moment we measure the bound fraction of the cluster, $f_{\rm bound}^{\rm 15Myr} = 0.14$ in this case. Later we will show how the bound fraction decreases with time and how this late measurement (to compare our results with previous work) affects our results.

5.3 Cases A and B: Keeping a Fixed Gas-Expulsion Time

To understand the relation between the embedded phase and the post-expulsion phase of a cluster we focus on three parameters: the Local Stellar Fraction (LSF), the bound fraction ($f_{\rm bound}$) and the virial ratio (Q).

The objective of this section is to test if the expulsion-time is a good indicator of the survivability of the cluster. We find that it is not. Instead, the LSF and $Q_{\rm f}$ at the moment of gas expulsion are much more important and decisive to predict the bound fraction.

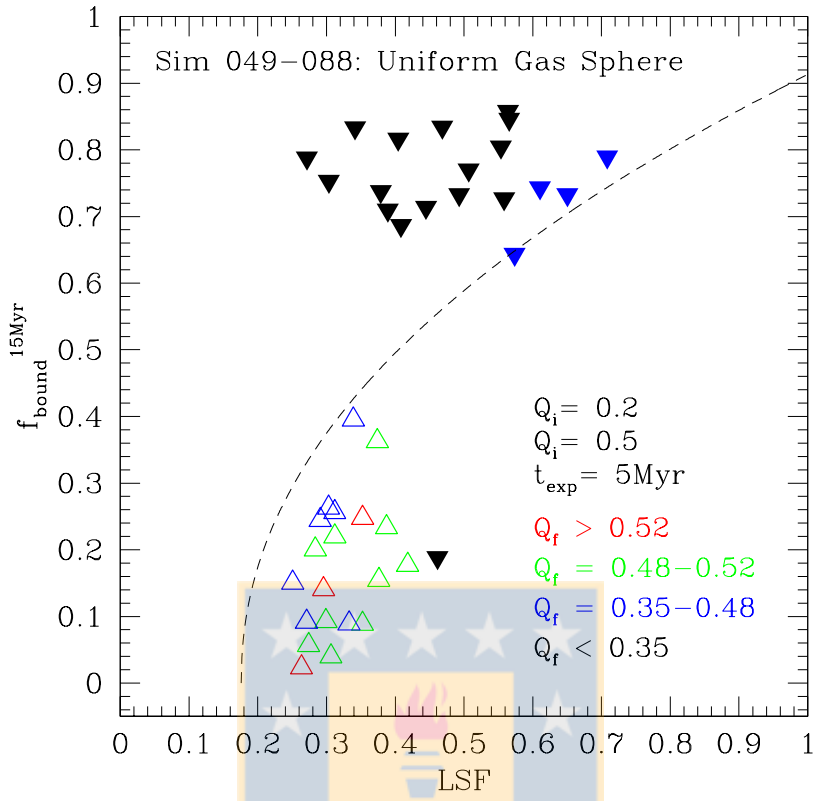

Figure 12: Results of case A. We show the bound fraction at 15 Myr $f_{\rm bound}^{\rm 15Myr}$ versus the $\rm LSF_{exp}$ measured at the expulsion time of $t_{\rm exp} = 5$ Myr. Downward pointing filled coloured triangles have initial virial ratios of $Q_{\rm i} = 0.2$ and upward-empty triangles have $Q_{\rm i} = 0.5$. The colours indicate the values of the virial ratio at the time of gas-expulsion $Q_{\rm f}$. All simulations use the same IMF-sample and the same fractal, varying the initial distribution of the masses. The dashed curve shows the trend for equal-mass simulations with $Q_{\rm f} = 0.5$ (Farias et al., in prep.).

In Fig. 12 we show the results for case A (simulations 49 to 88). We plot the bound fraction measured at 15 Myr $f_{\rm bound}^{\rm 15Myr}$ versus LSF measured at the moment of gas expulsion $t_{\rm exp} = 5$ Myr (all triangles). Here we choose one fractal distribution and one IMF-sample (sample 2). We then proceed to randomly assign the masses of our IMF sample to the stars within the fractal (RIP).

The trend for equal mass stars with $Q_{\rm f} = 0.5$ is shown as the dashed black curve. The initial virial ratio $Q_{\rm i}$ is denoted by the orientation of the triangles. The 'upward' triangles indicate a virial ratio $Q_{\rm i} = 0.5$ and 'downward pointing' triangles indicate a lower ratio of $Q_{\rm i} = 0.2$. The colours indicate the value of the virial ratio at the moment of gas-expulsion, ranging from 'cold' states (black), to 'hot' states (red). We find that the higher the LSF is, the higher the bound fraction will be, just as the simulations for equal mass particles indicate (Farias et al., in prep.). The opposite is also true, a low LSF gives a low bound

fraction. This behaviour can be understood taking into account that the LSF is a parameter for the concentration of the stars. Clusters with a high LSF have a high concentration, i.e. more mass in less volume, making a more tightly bound system that can better survive the gas-expulsion.

We also see in Fig.12 that the LSF is not the only important quantity. As the colours of the triangles indicate, low values for the virial ratios at the moment of gas expulsion favour higher bound fractions, grouping the results above the equal mass trend. And high virial ratios give low bound fractions, grouping the results under the curve. A high virial ratio indicates that the system has a high kinetic energy and/or a low potential energy, making it easier for the stars to leave the system when the gas expulsion happens.

The obvious result that cold initial conditions $Q_{\rm i} = 0.2$ increase the bound fraction is not quite obvious as we later see. In these results we rather see the combination of two effects, namely that colder initial conditions often lead to more compact star distributions, i.e. higher LSFs, at the time of gas-expulsion and therefore to a higher bound fraction as shown by the equal-mass curve. Secondly, as the colours of the triangles indicate, with our choice of expulsion time we catch the cold simulations at a virial state at the expulsion time which is below $Q = 0.5$ and therefore in a phase of contraction, which places them above the shown curve.

In Fig. 13 we show the temporal evolution of the LSF (*left panels*) and Q (*right panels*) for cases A and B. For demonstrative purposes we deactivate the gas expulsion so we can focus on what happens with the LSF and Q at the expulsion time. The *bottom panels* in Fig. 13 are the simulations with $Q_{\rm i} = 0.2$ and the *upper panels* are the ones with $Q_{\rm i} = 0.5$. With black we show the equal-mass simulation, and with red and blue the IMF-sample simulations, which use the same IMF-sample and the same fractal, but differ in the random initial positioning RIP. We see in the LSF that in the embedded phase of the cluster ($t < 5$ Myr) the IMF models have strong oscillations, with higher and lower peaks, compared to the equal mass model. Furthermore, we may see that the red and the blue curves are quite different, which must be attributed just to the different spatial mass distributions given by the RIP (as the fractal and sample are the same for both simulations).

We see in the left panels that if we start out with $Q_{\rm i} = 0.5$ we start out with low values of LSF which oscillate slightly and increase slowly with time from 0.25 to about 0.4. If we start with cold initial conditions $Q_{\rm i} = 0.2$ we start at the same low values of the LSF but the oscillations are much stronger (larger amplitude) and they seem to oscillate immediately around higher values (LSF ≈ 0.6). Therefore, it is obvious that it is more likely to catch a cold simulation at a higher LSF value at the given expulsion time than a simulation with $Q_{\rm i} = 0.5$.

These differences from simulation to simulation (even with the same initial parameters) generate a 'shift' of the curves. This shift causes, when the gas-expulsion happens at a fixed time, the LSF to have different values.

In the *right panels* of Fig. 13 we see the evolution of Q. In the *upper right* panel we observe that even if the systems start out of equilibrium with a value of 0.5, it oscillates around the virial equilibrium value ($Q_{\rm EQ} = 0.5$) trying to reach virialization until the gas-expulsion, when the system is strongly perturbed.

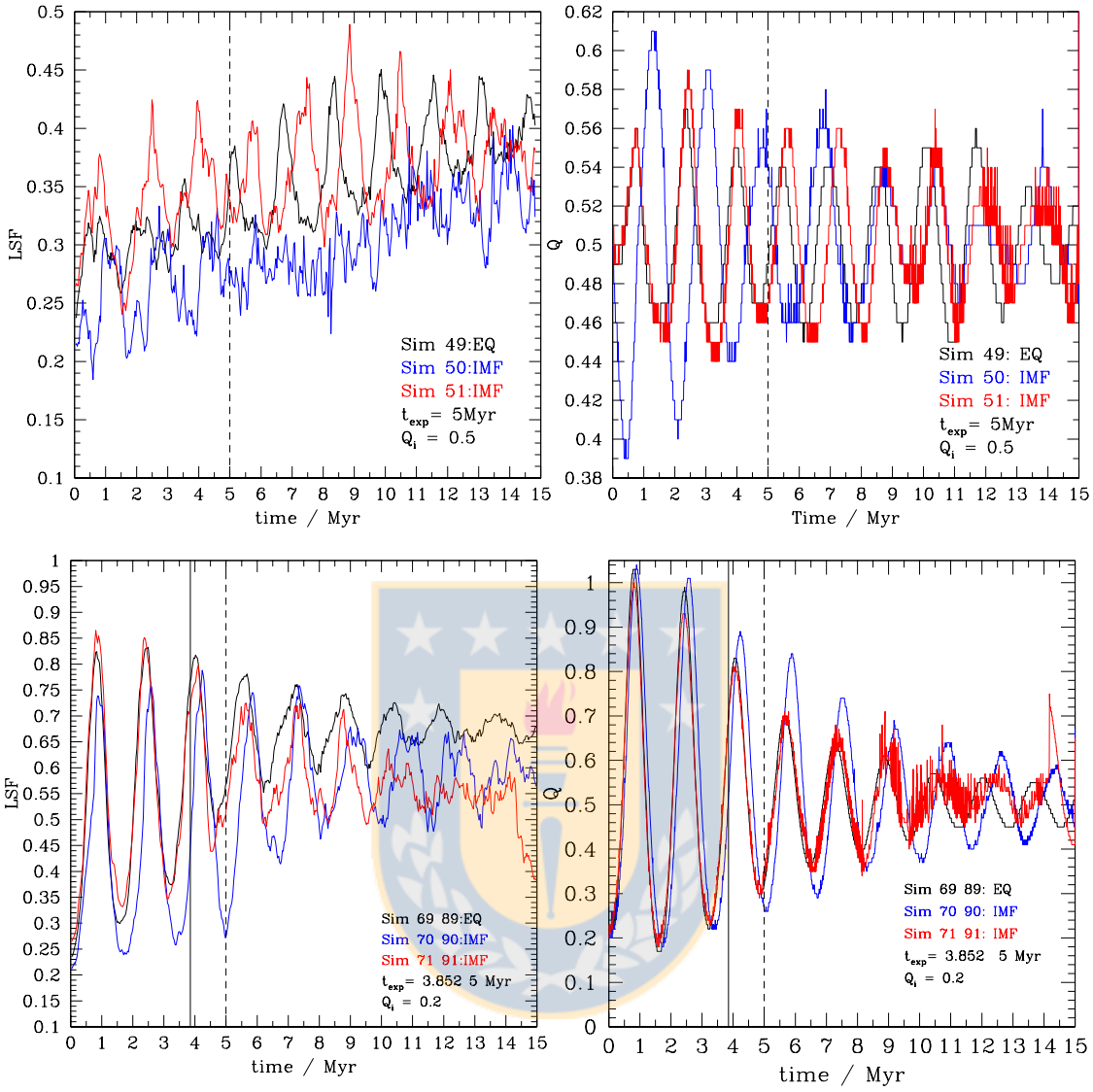

Figure 13: The LSF and Q versus time for sample simulations of cases A and B. For demonstrative purpose the gas expulsion is not activated in this simulations. All simulations in this figure use the same fractal distribution. The black curves indicate the equal mass simulations, the blue and the red use the same IMF-sample and the different colour indicate that they started with different 'random initial positioning' RIP. *Top-left:* LSF versus time for case A. The dashed vertical line indicates the expulsion time $t_{\rm exp} = 5$ Myr. We see that the LSF is fluctuating but slowly increases. *Top-right:* Q versus time for case A, with an initial virial ratio $Q_i = 0.5$. The dashed vertical line indicates the expulsion time. We see the slowly decaying oscillations in Q. *Bottom-left:* LSF versus time for cases A and B. The dashed vertical line indicates $t_{\rm exp} = 5$ Myr and the solid one a $t_{\rm exp} = 3.852$ Myr. *Bottom-right:* Q versus time for cases A and B, with an initial virial ratio $Q_{\rm i} = 0.2$. The dashed vertical line indicates $t_{\rm exp} = 5$ Myr (case A) and the solid one $t_{\rm exp} = 3.852$ Myr (case B).

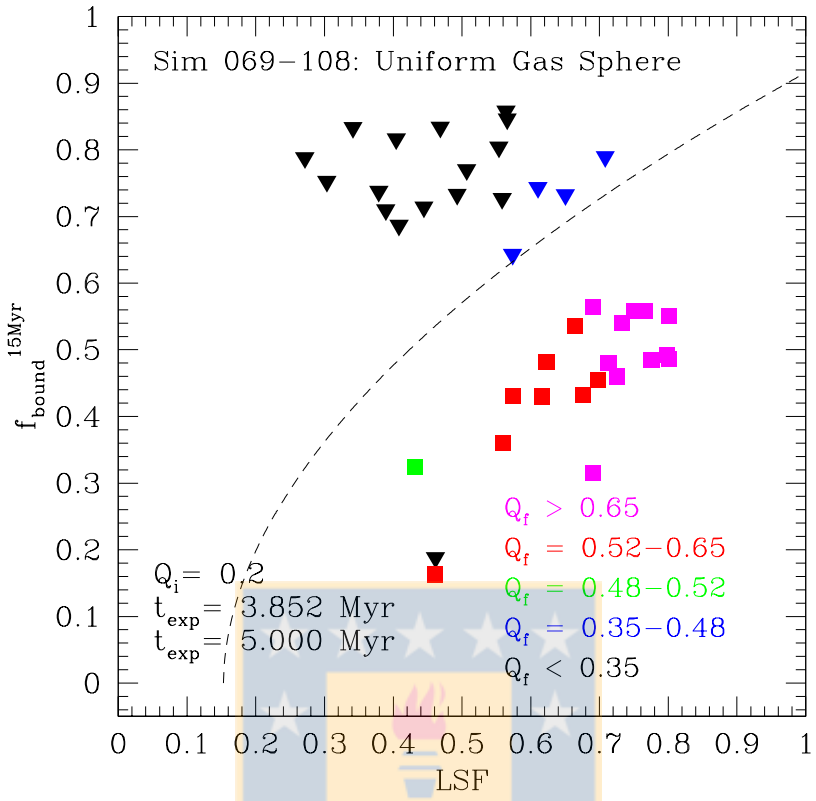

Figure 14: Results of case B. Bound fraction at 15 Myr $f_{\rm bound}^{\rm 15Myr}$ versus LSF measured at the expulsion time. All simulations here start with $Q_{\rm i} = 0.2$. Downward pointingfull coloured triangles indicate a expulsion time $t_{\rm exp} = 5$ Myr and the full coloured squares initicate $t_{\rm exp} = 3.852$ Myr. The colours indicate the value of the final virial ratio ($Q_{\rm f}$) at the time of gas expulsion. All simulations use the same IMF-sample. The dashed curve is the trend for equal-mass simulations (Farias et al., in prep.).

The amplitude of the oscillations of Q in the IMF models are stronger than in the equal mass model, which is more notorious in the $Q_{\rm i} = 0.2$ simulations (range of $\Delta Q \sim 0.8$), than in the ones with $Q_{\rm i} = 0.5$ ($\Delta Q \sim 0.2$).

In the panels for Q it is possible to observe several and sudden strong jumps of the Q curves, or 'spikes'. These spikes are generated by escaping stars, that gain enough kinetic energy (and therefore a high virial ratio) and leave the system.

When the gas-expulsion is activated these spikes are even more notorious. This means that there are more stars leaving the system, as there is no gas potential to support the cluster.

Like the LSF, the virial ratios at the expulsion time $Q_{\rm f}$ also change and are shifted to cold or hot values. This is more obvious in case B, where we use two expulsion times to compare, $t_{\rm exp} = 3.852$ and 5 Myr. We also note that the shift of Q is larger when $Q_{\rm i} = 0.2$ than when $Q_{\rm i} = 0.5$. This is because when $Q_{\rm i}$ is low, the whole system is collapsing and the overall properties are more important than the internal properties. When $Q_{\rm i} = 0.5$ the

internal effects become important and the distribution of the masses of the stars also become important.

The results of case B are shown in Fig.14. All simulations in the figure used the same fractal and the same IMF-sample and started with $Q_{\rm i} = 0.2$. The trend for equal mass stars with $Q_{\rm f} = 0.5$ is shown with the dashed black curve. The 'downward pointing' triangles are simulations with $t_{\rm exp} = 5$ Myr (same data as case A for $Q_{\rm i} = 0.2$). Squares are the simulations with $t_{\rm exp} = 3.852$ Myr. The colours indicate the values for $Q_{\rm f}$. Here we see clearly that for LSF in the range 0.56 and 0.76 different $Q_{\rm f}$ lead to different values of $f_{\rm bound}$; the higher (or lower) the virial ratio is, the lower (or higher) the bound fraction will be, revealing the inverse proportionally of the relation. Again the obvious result that shorter expulsion times lead to lower bound fractions is wrong. As we see in Fig. 13, if we use $t_{\rm exp} = 5$ Myr, we catch our simulations at a minimum in their Q-oscillations, leading to higher bound fractions, as in the case of the short expulsion time, where most simulations are closer to a maximum of their Q-oscillations. By shifting $t_{\rm exp}$ only 1.148 Myr the value of $Q_{\rm f}$ changes entirely. And a different value of $Q_{\rm f}$ moves $f_{\rm bound}$ to a higher or a lower value (Farias et al., in prep.).

Until now we have explored models with one fixed fractal distribution and one IMF-sample. We also fixed the expulsion time, and as a result the final virial ratio $Q_{\rm f}$ varies. We see how by introducing a random initial positioning of the masses of the stars we get different results even though we use the same fractal and IMF-sample. We also notice how important $Q_{\rm f}$ and LSF are to determine the bound fraction. In case D we come back to this model (fixed fractal and IMF-sample), but we fix the final virial ratio to $Q_f = 0.5$ to study the dependence of the bound fraction on the LSF.

5.4 Case C: Fixed Mass-Sample and Expulsion Time with Variable Fractal Distribution

We now analyse case C. The simulations use a single IMF-sample, but different fractal distributions with random initial positioning of the masses. In Fig. 15 we show the results in the LSF, $Q_{\rm f}$ and $f_{\rm bound}^{\rm 15Myr}$ spaces of case C. The trend for equal mass stars with $Q_{\rm f} = 0.5$ is shown with the dashed black curve. The 'upward-pointing-empty' triangles indicate results for initial virial ratios of $Q_{\rm i} = 0.5$ and the 'downward pointing-full' coloured triangles denote $Q_{\rm i} = 0.2$. The colours show the values for the virial ratios at the expulsion time $t_{\rm exp} = 5$ Myr.

Although in this case we change the fractal distribution in each simulation, the behaviour shown by previous cases stays the same; the bound fraction is inversely proportional to the virial ratio at the expulsion time and the LSF is proportional to the bound fraction. We now focus on $Q_{\rm f}$ values shown in blue and green with the range $Q_{\rm f} = 0.42$-0.52. Within this range the relation between LSF (for $Q_{\rm f} = 0.5$) and $f_{\rm bound}$ (dashed curve) for equal mass particles (Farias et al., in prep.) is reproduced by our simulations using an IMF.

We choose almost the same conditions as in case A: $t_{\rm exp} = 5$ Myr, $Q_{\rm i} = 0.2$, and $Q_{\rm i} = 0.5$, and we only change the random realization of the fractal distribution. Comparing

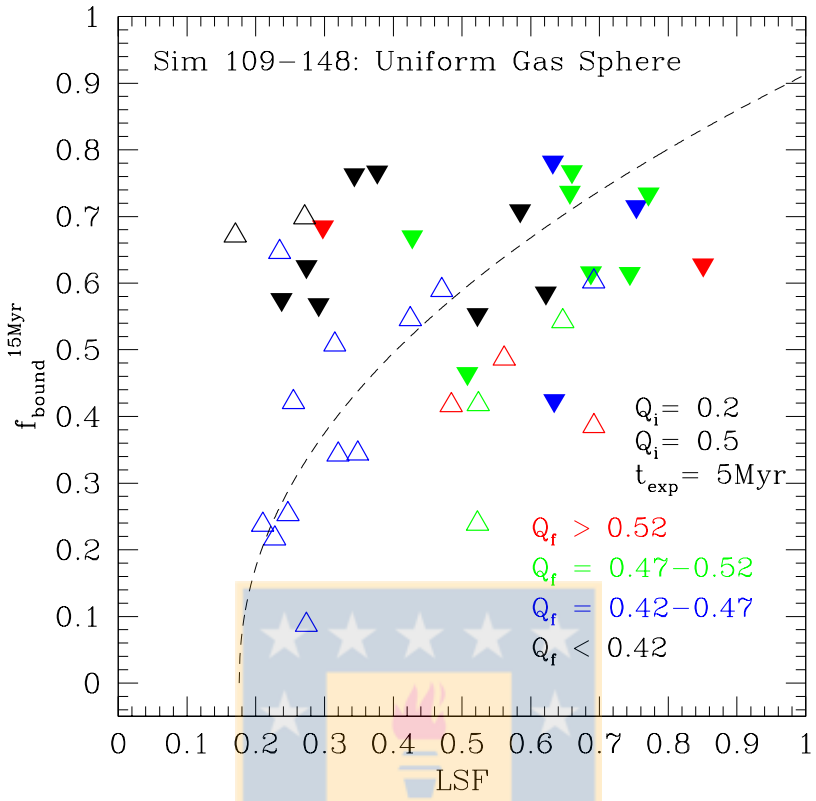

Figure 15: Results of case C. The bound fraction measured at 15 Myr $f_{\rm bound}^{\rm 15Myr}$ versus LSF at an expulsion time of $t_{\rm exp} = 5$ Myr. Downward pointing filled coloured triangles have initial virial ratios of $Q_{\rm i} = 0.2$ and each simulation is performed with different fractals. The upward-empty triangles use the same set of fractals, but they start with $Q_{\rm i} = 0.5$. The colours indicate the value of the virial ratio at the time expulsion $Q_{\rm f}$. The black dashed curve is the trend for equal-mass simulations (Farias et al., in prep.). All simulations use the same IMF-sample.

Fig. 12 with Fig. 15, we see a difference between cases A and C. The scatter of the results of case C is more evenly spread around the curve for equal mass stars, than in case A. The curves of Q versus time (oscillations) for low initial virial ratio $Q_{\rm i} = 0.2$ have larger shifts between each other than in case A, leading to a wider spread in the $Q_{\rm f}$ values.

We explain with case A that for low $Q_{\rm i}$ (collapsed) more global dynamics govern the behaviour of the cluster leading to stronger Q- and LSF-oscillations and therefore to a wider spread in LSF and $Q_{\rm f}$. Now additional scatter arises by using not only different mass assignations (RIP) but also using different random realizations for the fractal. In the equal mass study by Farias et al. (in prep.) we see that the results (using different random samplings for the fractals) scatter above and below the fitted curve. In case A we keep a fixed fractal, which may result in a bound fraction below or above the fitted curve (just using blue and green symbols with $Q_{\rm f}$ values close to 0.5). By varying the RIP we see that we introduce an

extra parameter for scatter just by randomly assigning the masses to different star positions. But, in the results of case A this additional scatter was not strong enough to distribute the single outcomes evenly above and below the fitted curve. Now we see that as soon as we vary the random realization of the fractal distribution we again see a scatter above and below the curve. We use this fact as a hint that the fitting curve by Farias et al. (in prep.) might be still valid if an IMF is introduced. We further investigate that in the next sections.

5.5 Case D: Fixed Final Virial Ratio $Q_{\rm f}$ at Gas Expulsion

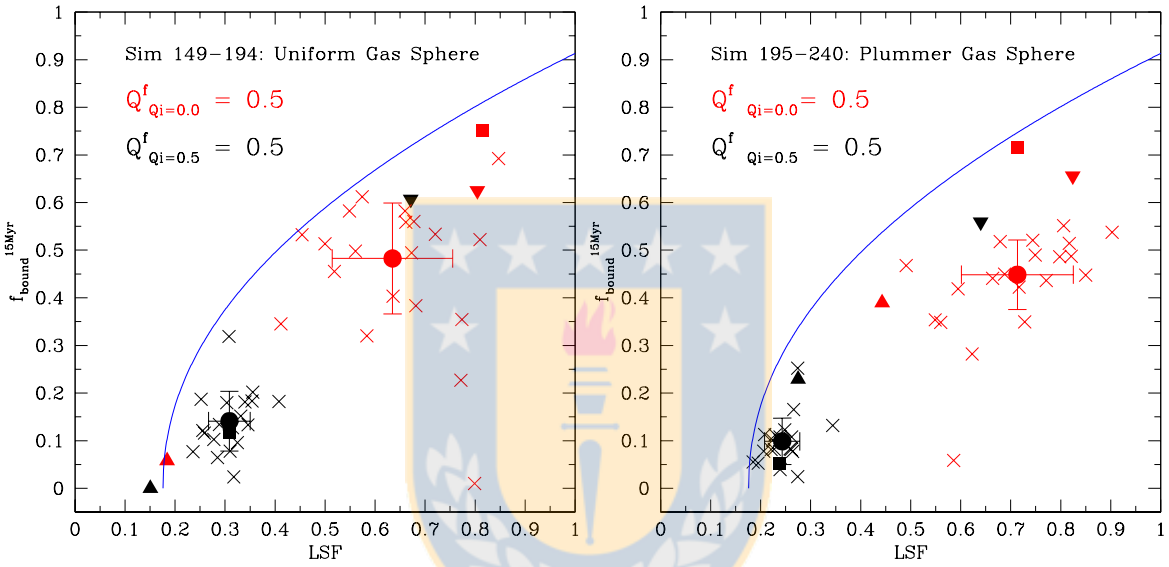

Figure 16: Results of case D. Bound fraction at 15 Myr ($f_{\rm bound}^{\rm 15Myr}$) versus LSF. The expulsion time varies between 1.8 and 3 Myr in order to obtain a fixed $Q_{\rm f} = 0.5$. The red symbols show initial virial ratios of $Q_{\rm i} = 0.0$ and the black are $Q_{\rm i} = 0.5$. The squares are the corresponding equal-mass simulations. Crosses have RIP but use the same fractal distribution. The downward pointing triangles are initially mass-segregated (most massive star in the centre) and the upward triangles are the inverse mass-segregated (least massive stars in the centre). The circles are the mean values of the crosses with one sigma error bars (the outliers are excluded and treated later). The *left panel* are the simulations with a uniform gas sphere and the *right panel* use a Plummer gas sphere. The blue curve is the trend for equal-mass simulations (Farias et al., in prep.).

In this case we have a setup similar to cases A and B. All simulations use the same IMF-sample and the same fractal distribution and two sets for the initial virial ratio $Q_{\rm i}$, but here we fix the final virial ratio at the expulsion time $Q_{\rm f}$.

We show the results of case D in Fig. 16, plotting the bound fraction at 15 Myr ($f_{\rm bound}^{\rm 15Myr}$) versus the LSF. As we see in Fig. 13 the evolution of Q is different for each simulation.

Therefore, to ensure to have the same $Q_{\rm f} = 0.5$ in each simulation we have to vary the time of gas-expulsion slightly from 1.2 Myr to 3 Myr. The red symbols show initial virial ratios of $Q_{\rm i} = 0.0$ and the black are $Q_{\rm i} = 0.5$. The squares are the corresponding equal-mass simulations using the same fractal distribution. Crosses have random initial mass distributions. The 'downward pointing' triangles represent initially maximum mass segregated simulations. This means that we sort the masses and place the most massive star closest to the centre of the fractal, then the next massive star and so on until the least massive star is furthest away from the centre. The 'upward' triangles are the inverse mass-segregated (less massive stars in the centre and most massive at the outskirts). The circles are the average values of the crosses (the outliers are excluded and treated later). The *left panel* are the simulations with the stars embedded in a uniform gas sphere and in the *right panel* we show the ones embedded in a Plummer gas sphere. The blue curve is the trend for equal-mass simulations (Farias et al., in prep.).

We see again in Fig. 16 that for models with $Q_{\rm i} = 0.5$ (black symbols) we get low LSF values and therefore low bound fractions. We remark that the scatter is evenly distributed around the equal mass simulation (black square) and so we assume that the reason for all simulations being below the fitting line is that the corresponding equal-mass case falls short of the mean trend.

The mass segregated (downward pointing black triangle) and inverse-mass segregated (upward black triangle) simulations strongly deviate from the random distributions, but they still follow the trend for equal mass particles (blue curve). We see that in principle the maximum segregated simulations always lead to very high LSF values and therefore to higher bound fractions. The inverse mass-segregated simulations follow either the cloud of random placement results or even lead to a complete destruction of the star cluster $f_{\rm bound} = 0$ for the uniform gas sphere case.

For the models with $Q_{\rm i} = 0.0$ (red symbols) which lead to higher values of LSF, the scatter is preferentially distributed at lower values than the equal mass simulation (red square) and also is distributed far below the trend for equal mass particles. Here we seem to strongly deviate from the general trend of results found by Farias et al. (in prep.) for equal-mass stars. We will explain this behaviour with the study of case F.

The initially high mass segregated simulations (downward pointing triangles) again lead to higher LSF and therefore to higher bound fractions than the bulk of the RIP simulations. And again the inverse mass-segregated simulations lead to lower LSFs and therefore to lower bound fraction than the bulk of the RIPs. Once again we see an almost destroyed cluster in the case of a uniform sphere gas potential.

5.6 Case E: Fixed $Q_{\rm f}$ but Different IMF-Samples

In this case we vary not only the IMF samples, using 10 different samples with properties shown in Table 2 (IMF$_{sample}$ 2 to 12.), but also vary the random realizations of of the fractal distribution. We give an overview of some results in Table 5.6.

The results of case E in Fig. 17 show the bound fraction at 15 Myr $f_{\rm bound}^{\rm 15Myr}$ versus LSF. The expulsion time varies between 1.2 and 3 Myr to ensure $Q_{\rm f} = 0.5$. The red symbols show

Table 3: Results of case E (uniform gas sphere only). Simulations shown here have $Q_{\rm f} = 0.5$ and $Q_{\rm i} = 0.0$. The first 10 rows are IMF mass samples, each with a different fractal, and the next 10 rows are the respective same fractal, but with equal mass particles. For the mass distribution we use a random initial positioning RIP.

Simulation	$t_{\rm exp}$ [Myr]	Type	$N_{\rm tot}^{\rm stars}$ [n^o]	$M_{\rm tot}^{\rm stars}$ [M$_\odot$]	LSF	$f_{\rm bound}^{\rm 15Myr}$
Sim 261	3.053	IMF(03)	948	500.06	0.2861	0.2602
Sim 262	2.577	IMF(04)	906	500.31	0.4858	0.3594
Sim 263	1.653	IMF(05)	972	500.32	0.4625	0.4009
Sim 264	2.045	IMF(06)	816	500.03	0.4788	0.6013
Sim 265	2.801	IMF(07)	1010	500.74	0.5656	0.5609
Sim 266	1.681	IMF(08)	1064	500.31	0.3495	0.4969
Sim 267	1.709	IMF(09)	1005	500.40	0.4654	0.6049
Sim 268	2.941	IMF(10)	705	500.42	0.5449	0.3388
Sim 269	1.989	IMF(11)	789	500.01	0.4104	0.4853
Sim 270	1.709	IMF(12)	1018	500.80	0.3120	0.5368
Sim 271	2.703	Eq. Mass	948	500.06	0.3099	0.1181
Sim 272	2.409	Eq. Mass	906	500.31	0.6148	0.6744
Sim 273	1.597	Eq. Mass	972	500.32	0.4181	0.5669
Sim 274	1.961	Eq. Mass	816	500.03	0.5733	0.3848
Sim 275	1.597	Eq. Mass	1010	500.74	0.7973	0.6505
Sim 276	1.709	Eq. Mass	1064	500.31	0.3691	0.6654
Sim 277	1.667	Eq. Mass	1005	500.40	0.5261	0.6925
Sim 278	1.989	Eq. Mass	705	500.42	0.3750	0.3915
Sim 279	1.947	Eq. Mass	789	500.01	0.3487	0.2649
Sim 280	1.709	Eq. Mass	1018	500.80	0.3557	0.6297

initial virial ratios $Q_{\rm i} = 0.0$ and the black symbols represent $Q_{\rm i} = 0.5$. The squares are the equal-mass simulations and the crosses the corresponding simulations using different IMF samples. The IMF-sample simulations have a random initial positioning of the masses. The *left panel* are the simulations with a uniform gas sphere and the *right panel* use a Plummer gas sphere. The blue curve is the trend for equal-mass simulations (Farias et al., in prep.).

From the plot we see that the equal mass simulation (squares) are scattered around the trend (blue curve) as expected. For the IMF simulations (black crosses) the scatter at low and intermediate LSF is distributed around the the equal mass simulations (black squares). Therefore, we see that the scatter introduced by different IMF samples does not affect the main trend found for equal mass particles, as we do not see a profound change comparing with case C.

For higher values of LSF (red crosses) we do see a drop of the bound fraction, the results preferentially distributing below the distribution of the equal mass simulations (red squares) and below the curve. In the next section we present arguments that this is due to the internal

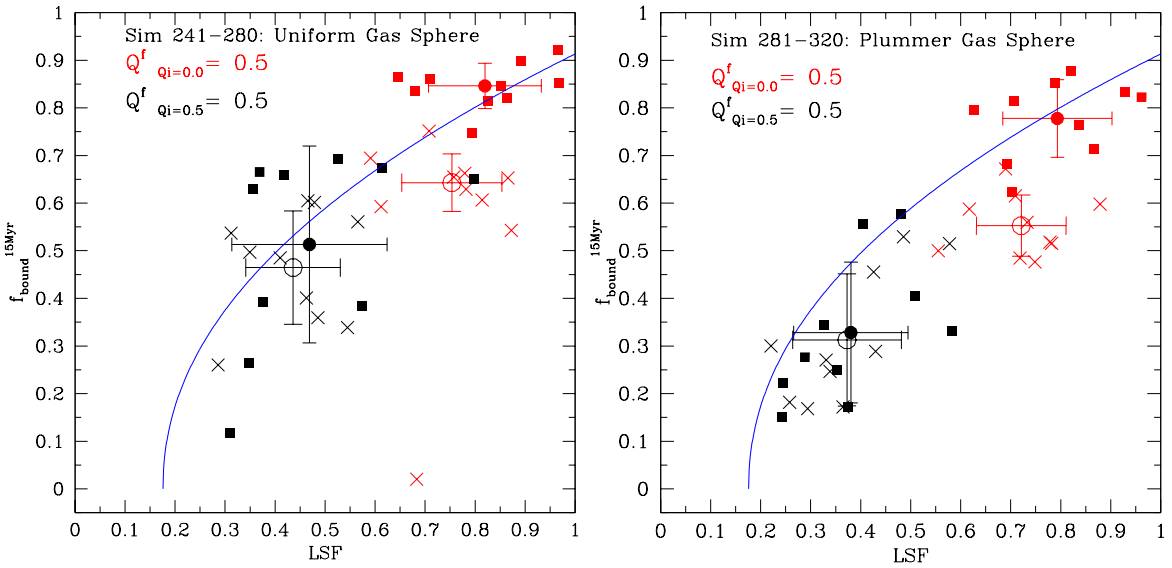

Figure 17: Results of case E. Bound fraction at 15 Myr $f_{\rm bound}^{\rm 15Myr}$ versus LSF. The expulsion time varies between 1.8 and 3 Myr. The red symbols indicate an initial virial ratios of $Q_{\rm i} = 0.0$ and the black symbols indicate a $Q_{\rm i} = 0.5$. The squares represent the equal-mass simulations and the crosses are simulations with different IMF samples. Each pair of simulations use a different fractal distribution. *Left panel*: simulations using a uniform gas sphere; *Right panel*: simulations using a Plummer gas sphere. The blue curve is the trend for equal-mass simulations (Farias et al., in prep.). The circles are the mean values with one sigma error bars. The empty circles correspond to the IMF simulations, and the full-coloured circles correspond to the equal-mass simulations.

evolution of the cluster after gas expulsion rather than a change in the general trend proposed by Farias et al. (in prep.).

5.7 Case F: Time Evolution of the Bound Fraction and Ejections

In this section we analyse in more detail the time-dependence and the dynamical evolution in our simulations.

In Fig. 18 we show the evolution of the bound fraction with time after the gas-expulsion. As the expulsion times range from 1.2 to almost 3 Myr we start the measurements of the bound fraction at 3 Myr, and continuos until 15 Myr. We use the simulations from case D, which have a uniform gas sphere. The red lines indicate simulations with $Q_{\rm i} = 0.0$ and the black indicate $Q_{\rm i} = 0.5$. In the *left panel* we plot with solid lines, the bound fraction measured at different times $f_{\rm bound}$ for each simulation. The dashed lines (black and red) are the equivalent equal-mass simulations. For better visibility we plot in the *right panel* the mean values (excluding outliers, which we discuss separately below) of the simulations together with the equal-mass simulations again.

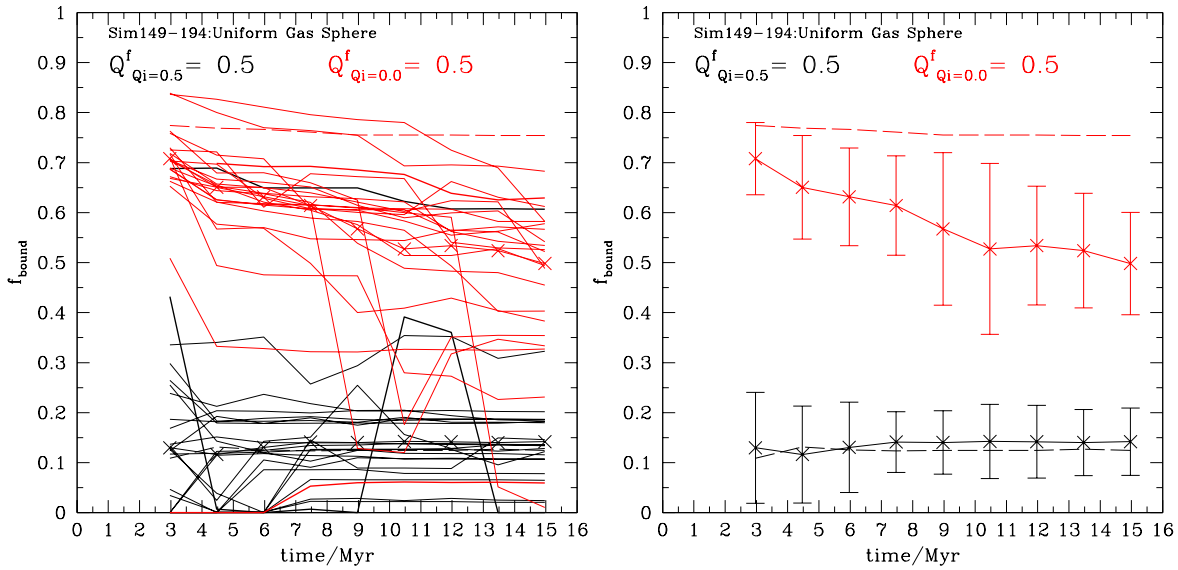

Figure 18: Final bound fractions $f_{\rm bound}$ measured at different times after the gas-expulsion for the simulations of case D. The simulations use a single IMF-sample and the same fractal distribution. The red lines indicate simulations with initial virial ratios of $Q_{\rm i} = 0.0$ having high LSF and $f_{\rm bound}$ values and the black lines indicate simulations starting with $Q_{\rm i} = 0.5$, leading to lower LSF and $f_{\rm bound}$ values. The virial ratio at the gas-expulsion time is kept constant at $Q_{\rm f} = 0.5$. *Left panel*: solid lines show the bound fraction measured at different times for each simulation. The dashed lines (black and red) are the corresponding equal-mass simulations. *Right panel*: we plot $f_{\rm bound}$ versus time. The dashed lines are the equal mass simulations and the solid lines with crosses are the average values from all simulations calculated without the outliers and are plotted with one sigma error bars.

In case D we observe in Fig. 16 that the scatter in the simulations with $Q_{\rm i} = 0.5$ with low LSF and $f_{\rm bound}$ values (black crosses) were distributed around the equal mass simulation, while the simulations with $Q_{\rm i} = 0.0$ leading to higher LSF and $f_{\rm bound}$ values are distributed below the equal-mass trend. This could lead to the impression that as soon as we introduce a mass-spectrum to our stars the bound fractions at high LSF are significantly lower therefore leading to less massive surviving clusters.

In Fig. 18 we now observe the true reason for this finding. In our studies we chose to measure the final bound fraction of the star cluster at a relatively late time of 15 Myr to make sure that we wait long enough (a few crossing times of the remaining cluster) to ensure to see the new equilibrium or quasi-equilibrium distribution and not an object suffering from the aftermath of gas-expulsion. As long as we use equal masses in our previous studies this procedure was not a problem as two-body encounters in equal-mass simulations are not as violent as encounters between high and low mass stars. The dashed lines (equal-mass) in the right panel of Fig. 18 are almost horizontal, i.e. the cluster loses stars very slowly, even for high density clusters (red line). As soon as we introduce an IMF, our remaining cluster

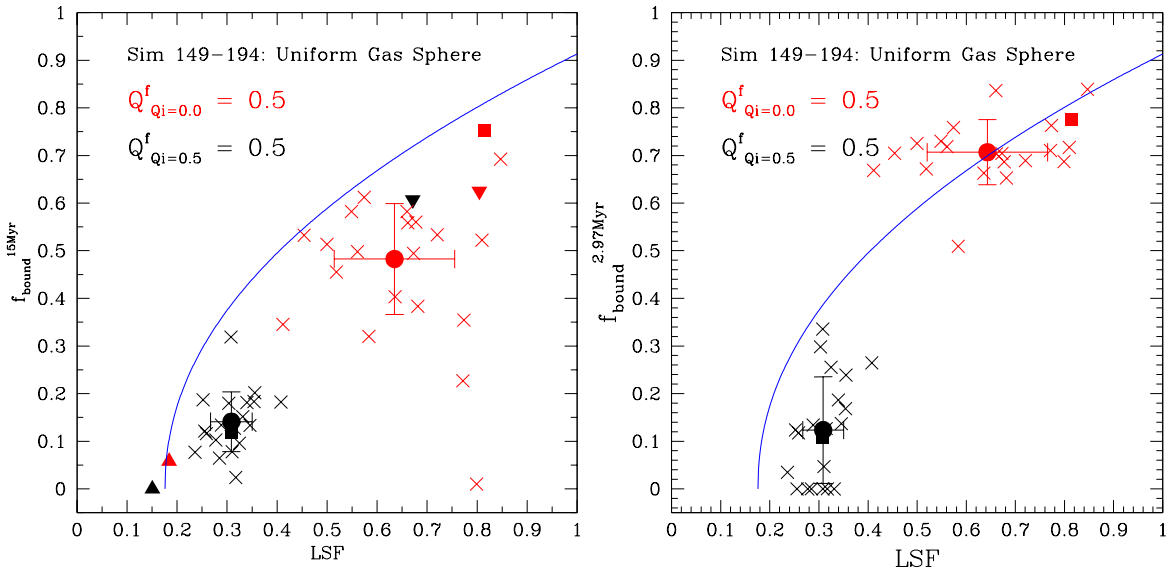

Figure 19: Results of cases D and F. The bound fraction versus LSF. The red symbols show initial virial ratios of $Q_{\rm i} = 0.0$ and the black symbols represent $Q_{\rm i} = 0.5$. Squares show the equal-mass simulations. Crosses are the simulations with RIP. The downward pointing triangles are the initially maximum mass segregated and the upward triangles are the inverse mass-segregated (low mass stars in the centre) simulations. The circles are the mean values of the crosses with one sigma error bars (the outliers are excluded). All simulations use the same initial fractal distribution. *Left panel*: the bound fraction measured at 15 Myr $f_{\rm bound}^{\rm 15Myr}$. *Right panel*: same simulations but the bound fraction is measured at 2.97 Myr $f_{\rm bound}^{\rm 2.97Myr}$. The simulations use a uniform gas sphere. The blue curve is the trend for equal-mass simulations (Farias et al., in prep.).

suffers from high-speed ejections of stars and the bound mass decreases faster. While in the low-density environment (at low bound fractions = simulations with $Q_{\rm i} = 0.5$, black line) the bound fraction still stays constant, we see a rapid decline in the bound fraction at high density clusters (high bound fraction = simulations with $Q_{\rm i} = 0.0$, red line).

If we measure the bound fraction long after the gas-expulsion, i.e. at 15 Myr, we measure a reduced bound fraction due to internal two-body evolution and not necessarily the original number of stars which are forming a bound object after the gas is expelled. Therefore, we see the red crosses in Figs. 16 and 17 and in the left panel of Fig. 19 all lie below the corresponding simulations with equal-mass stars.

If we measure the bound fraction immediately after the gas-expulsion at $t = 2.97$ Myr ($f_{\rm bound}^{\rm 2.97Myr}$; right panel of Fig. 19), i.e. before internal evolution is able to decrease the bound mass of the cluster significantly, we see that the red crosses shift upwards and now scatter around the equal-mass curve, as expected.

Finally, in this section we have to deal with simulations we dub 'outliers', i.e. simulations which present a high LSF and very low or even zero bound fractions. The 'outliers' of Fig. 16

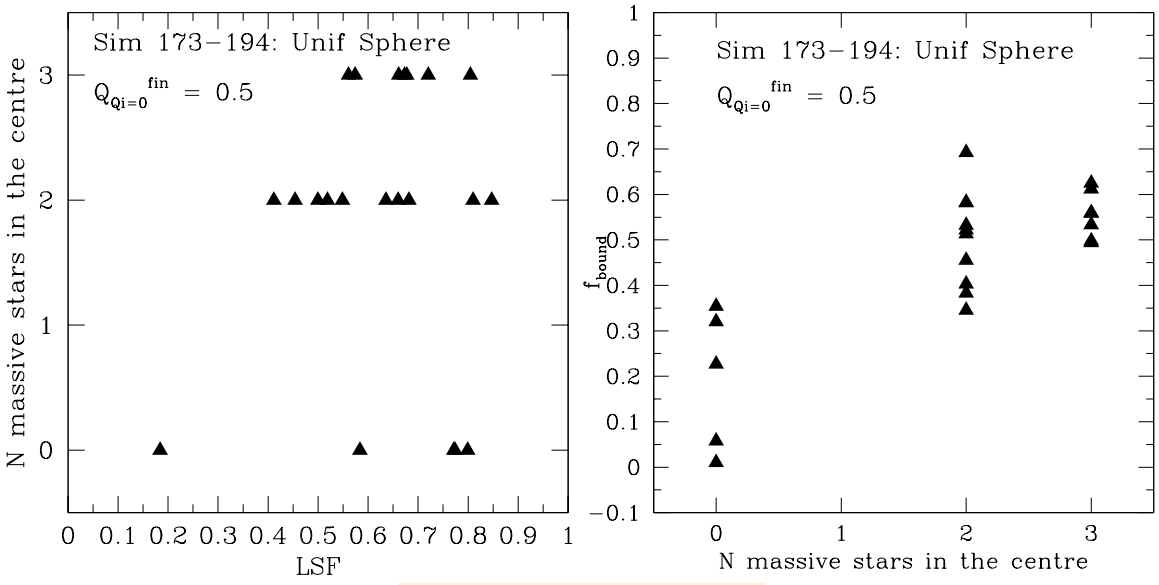

Figure 20: Results of case D. This used IMF sample has three very high mass stars ($m > 10$ M$_\odot$). *Left panel:* We plot the remaining number (within the cluster, N) of the three most massive stars at 15 Myr versus the LSF. *Right panel:* We plot $f_{\rm bound}^{\rm 15Myr}$ versus N.

are simulations which looking at the time dependence in the left panel of Fig. 18 (red solid lines) have sudden drops of the bound fraction to very low values.

The IMF-sample used in these simulations contains 3 very massive stars. We check all the simulations with $Q_{\rm f} = 0.5$ to test for differences. We find that the outlier systems suffer from 'ejections' of their 3 most massive stars. We show this in Fig. 20, where we quantify and plot the remaining of the 3 most massive stars against LSF and $f_{\rm bound}^{\rm 15Myr}$. From these 3 stars we find in our systems that either 0, 2 or 3 are left (never just one). Usually two of these stars form a very tight binary system in the centre of the remaining cluster. If the third star is present a triple usually formed. Two are very close and the third is always further away. This triple system contains a significant fraction of the remaining bound mass. Systems with all of the three most massive stars present are consequently amongst the systems with the highest bound fractions (as the bound fractions count the mass in stars and not numbers).

Through body encounters the third star sometimes gets a kick and leaves the system and only the hard binary remains. This configuration is the second most massive configuration. The central binary contains a lot of mass, therefore raising the bound mass fraction. But some systems experience body encounters between the three most massive stars leading to one star experiencing a high-velocity kick and therefore leaving the system and the binary experiencing a recoil which still is energetic enough for the binary to leave the remaining bound cluster. Now the remaining system is deprived of a significant fraction of its remaining mass, left out of equilibrium, and as a result many stars more become unbound and leave the system. In some systems this leads to a complete dissolution of the cluster.

As we always see that two of the most massive stars form a central binary, there are no

results in which only one of the three stars is left in the system.

We see in the *left panel* of Fig. 20 that the range for high LSF is mostly populated by the binary system, then the triplet and only a few without the three massive stars. In the *right panel* we see a more clear trend, showing that the simulations that are 'outliers', lack on the presence of these 3 high mass stars. This suggests that the presence of high mass stars is essential for the survival of our clusters. On the other hand a hard and massive binary in the centre also accelerates the internal evolution by efficiently kicking other stars out of the system.

We must remember that these are idealized models and according to stellar evolution these massive stars would have disappeared a long time ago as supernovas (causing of the gas-expulsion!).

5.8 Case G: Primordial or Initial Mass Segregation

In this case we further explore primordial or initial mass-segregation. For that, we use the same procedure and set of IMF samples and fractal distributions that were use for case E. Instead of randomly positioning the stars within the cluster, we position the most massive stars in the centre and the less massive stars in the outskirts of the cluster, generating a maximum initial mass-segregation. We show the results in the panels of Fig. 21. The red symbols show initial virial ratios of $Q_{\rm i} = 0.0$ and the black symbols are $Q_{\rm i} = 0.5$. The squares represent the equal-mass simulations and the triangles are the initially maximum mass segregated simulations. In the *left panel* we show the bound fraction measured at 4.47 Myr ($f_{\rm bound}^{4.47{\rm Myr}}$) and in the *right panel* the bound fraction measured at 15 Myr ($f_{\rm bound}^{15{\rm Myr}}$). The blue curve is the trend for equal-mass simulations (Farias et al., in prep.).

The first thing we notice in the *left panel* is that just after the gas expulsion, the bound fraction for the IMF simulations (triangles) are scattered around the equal-mass trend and of course the equal mass simulations (squares) also follow the trend. We also see that introducing an IMF distribution and an initial mass segregation produce two effects depending on the initial virial ratio. In the simulations with $Q_{\rm i} = 0.5$ (black symbols) we have that the bound fraction and the LSF in the simulations with initial mass segregation (black triangles) get shifted to higher values following the trend. This is because in these systems the stellar mass is more concentrated than in the equal-mass systems. On the other hand, for the simulations with $Q_{\rm i} = 0.0$ the initially mass segregated simulations (red triangles) are shifted to lower values and following the equal-mass trend. This is due to the strong dynamical evolution of the cluster previous to the gas expulsion. We have already seen in the previous section how fast the temporal evolution of the simulations with an IMF are, compared with the equal mass simulations. When the resulting bound fraction is high, it also means that the concentration is high (high LSF) and the resulting difference with the equal-mass simulation is larger. Therefore, the massive stars in the embedded phase of the IMF simulations make the cluster less concentrated and decrease the bound mass fraction, but still following the equal-mass trend.

In the *right panel* we again see the effects of dynamical evaporation. Here the bound fraction is also shifted, but only in the $f_{\rm bound}$-axis. As noticed in the previous case, this

effect is also stronger at LSF ~ 0.6 and higher. We also notice one outlier at LSF ~ 0.71 and $f_{\rm bound}^{\rm 15Myr} \sim 0.23$ (black triangle). Contrary to the previous outliers that are caused by ejection of massive stars, in this case the cluster happens to get divided in two clusters. An as we always measure the most massive remaining cluster we got a low bound fraction $f_{\rm bound}^{\rm 15Myr} \sim 0.23$.

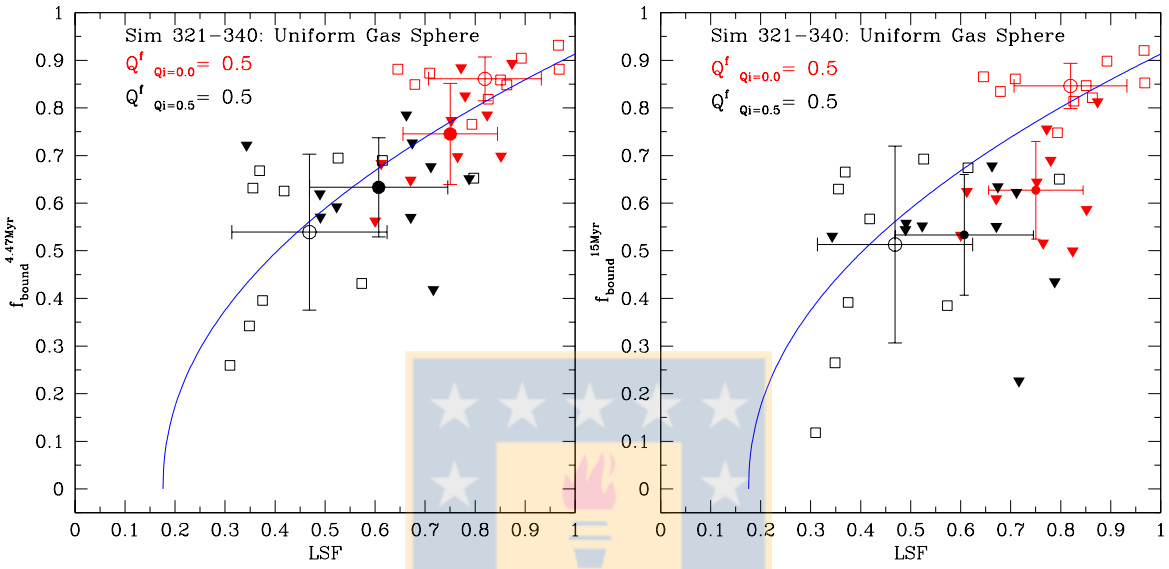

Figure 21: Results of case G. LSF versus the bound fraction measured at different times. Here we use the same set of IMF samples and fractals used for case E (Ten different IMF samples, each with a different fractal distribution). The difference with case E is that here we position the massive stars in the centre and the less massive in the outskirts of the cluster, generating an initial mass-segregation. Fixing the final virial ratio $Q_{\rm f} = 0.5$, we get an expulsion time that varies between 1.8 and 3 Myr. The red symbols show initial virial ratios of $Q_{\rm i} = 0.0$ and the black symbols are $Q_{\rm i} = 0.5$. The squares represent the equal-mass simulations and the triangles are the initially maximum mass segregated. *Left panel*: the bound fraction measured at 4.47 Myr ($f_{\rm bound}^{\rm 4.47Myr}$); *Right panel*: the bound fraction measured at 15 Myr ($f_{\rm bound}^{\rm 15Myr}$). The blue curve is the trend for equal-mass simulations (Farias et al., in prep.).The circles are the mean values with one sigma error bars. The empty circles correspond to the equal-mass simulations. The full-coloured circles correspond to the IMF simulations.

6 Conclusions and Outlook

The absence of old (> 10 Myr) low mass star clusters suggests that there is a universal early destruction mechanisms that generates 'Infant Mortality' of star clusters. Previous studies made with simulations (Weidner et al. (2010), Smith et al. (2012), and others) concluded that the gas-expulsion of embedded star clusters is an effective mechanism to explain the 'Infant Mortality'.

An important parameter for star clusters postulated by Lada & Lada (2003) is the Star Formation Efficiency (SFE), which helps to estimate the survivability of the cluster and quantifying the final bound fraction $f_{\rm bound}$. Weidner et al. (2010) find a relation that enables one to predict the final bound fraction by just measuring SFE. But that study uses the assumption of virial equilibrium and a smooth distribution for the stars. With these assumptions the authors obtain no surviving star clusters for a SFE $= 0.2$ under a rapid mass loss rate for the gas.

Smith et al. (2012) use clusters with a SFE $= 0.2$ and an initially clumpy and out of equilibrium distributions and obtain surviving clusters. They introduce the Local Stellar Fraction LSF and find new relations that help to predict the survivability of star clusters. Farias et al. (in prep.) find a trend between the final bound fraction and the LSF for simulations with $Q_{\rm f} = 0.5$. But, all these previous studies from our group were made with equal mass stars.

In this project we explore how the introduction of an Initial Mass Function affects the behaviour and results previously found for clusters with equal mass stars. For that we proceed varying different parameters, one or two at the time. This give us seven cases: A to G.

In cases A and B we explore models with one fixed fractal distribution and one IMF-sample. We also fix the expulsion time, and as a result the final virial ratio $Q_{\rm f}$ varies. We could see how just by introducing a random initial positioning for the masses of the stars we get different results considering even that we use the same fractal and IMF-sample. We also notice how important Q and LSF are to determine the bound fraction.

In case C we change the fractal samples obtaining a scatter of the results that is more evenly spread around the curve for equal mass stars than the scatter in case A. The curves of Q versus time for low initial virial ratio $Q_{\rm i} = 0.2$ have larger shifts with each other than in case A. For low $Q_{\rm i}$ (colapse) global properties govern the dynamics in the cluster more than internal properties such as the position of the masses within the fractal. Therefore, changing the fractal we change the cluster in a more global way than just by changing the position of the masses. For low initial virial ratio $Q_{\rm i}$ the scatter introduced by different fractals sums to the scatter introduced just by the RIP, obtaining a bigger scatter.

In case D we find that for models with $Q_{\rm i} = 0.5$ we get low LSFs and low bound fractions. We remark that the scatter is evenly distributed around the equal mass simulation. The mass segregated and inverse-mass segregated simulations strongly vary from the distribution of results, but they still follow the trend for equal mass particles. For the models with high LSF and $Q_{\rm i} = 0.0$ the scatter is preferentially distributed at lower values than the equal mass simulation (red squares) and also distributed below the trend for equal mass particles. Later in case F we explain the cause of this. The initially high mass segregated simulations (downward pointing triangles) are high concentrated independent of the initial virial ratio

used.

In case E we see that the equal mass simulations are scattered around the trend as expected: the higher the LSF the higher the bound fraction. For the IMF simulations the scatter at low and intermediate LSF is distributed around the the equal-mass simulations as well. Therefore, we see that the scatter introduced by different IMF samples does not affect the main trend found for equal mass particles, as we do not see a profound change comparing with case C. For higher LSF we do see a drop of the bound fraction, distributing the results preferentially below the distribution of the equal mass simulations and below the trend curve. The cause for this becomes clearer when we analyse the time evolution of the bound fraction in case F.

We see in case F that the bound fraction at high LSFs, i.e. for low initial virial ratios $Q_{\rm i} = 0.0$ has a large scatter significantly below the equal mass simulations. The reason for this behaviour is that these systems are quite dense and therefore exhibit a rapid internal evolution. While, shortly after gas-expulsion exhibiting the same bound fractions than the equal-mass simulations would predict, their internal evolution is that fast that if we measure the bound fraction after several crossing-times, as we do in the equal-mass simulations, the bound fraction has decreased by a significant amount.

In some cases, we dub 'outliers', the bound fraction even drops to values close or equal to zero. We identify these cases as the simulations in which all of the massive stars (3 in the IMF sample used) have left the system after a triple-encounter. The systems with the highest bound fractions have all those 3 massive stars still present in the system forming a triple system. Other intermediate outcomes of our simulation still exhibit a massive binary in the centre. This massive binary is always present and therefore we see no simulation with just one remaining bound massive star. We also notice one outlier caused by one remaining cluster that get divided into two less massive clusters.

We also note that the random initial positioning introduce another factor of stochasticity in the results. If we use maximum mass-segregated distributions, we obtain very high values of LSF (as all the most massive stars are in the central area from the beginning) and therefore also high bound fractions. If we use the inverse mass-segregated distributions we see that the cluster has almost no chance to survive at all. So, the mass-segregation influences the resulting LSF at the time of gas-expulsion following the trend for the equal-mass simulations.

In future researches the Weidner limit for the maximum mass of the stars will be introduced. This would forbit samples with high mass stars. We also will introduce a more complete dynamical analysis for the cluster, studying the trend between the final bound fraction vs. LSF for different final virial ratios, $Q_{\rm f} = 0.2$ and 0.7 etc.

CHAPTER II

7 The Dwarf Spheroidal Galaxies Leo IV and Leo V: A bound pair?

7.1 Abstract

The dwarf spheroidal (dSph) galaxies are thought to be the most dark matter (DM) dominated objects known. Leo IV and Leo V are two ultra-faint dwarf spheroidal galaxies recently found around the Milky Way. Their distances to the Milky Way are 154 kpc and 175 kpc respectively. Their rather short difference in radial distance and the fact that they also have a small projected distance on the sky led to the idea that we might see a new pair of gravitationally bound galaxies - like the Magellanic Clouds. Our results show that the minimum total dark matter mass required for the pair to be bound has to be between $1.6 \times 10^{10} M_{\odot}$ and $5.4 \times 10^{10} M_{\odot}$ (within the virial radius). Computing the mass of dark matter within a standard radius of 300 pc shows that our models are within the predicted range of dark matter content for satellites that faint. We therefore conclude that it could be possible that the two galaxies constitute a bound pair.

7.2 Introduction

Many new faint dwarf spheroidal (dSph) galaxies have been discovered around the Milky Way (MW) (e.g. Willman et al., 2005; Zucker et al., 2006; and many more). Many of those dwarfs are less luminous than star clusters and their stars exhibit high velocity dispersions (e.g. Simon & Geha, 2007). If these objects are in virial equilibrium then their luminous masses do not explain their high velocity dispersion, and this would imply that these objects are the most dark matter (DM) dominated objects known in the universe. They would exhibit high mass-to-light (M/L) ratios, in the order of hundreds (e.g. Simon & Geha, 2007) or even thousends for some cases. In this project we focus on two of these new ultra-faint dwarfs, namely Leo IV (Belokurov et al., 2007) and Leo V (Belokurov et al., 2008). Their properties are studied by many authors: for Leo IV: (Moretti et al., 2009; Simon et al., 2010; Sand et al., 2010) and for Leo V: (Walker et al., 2009a,b). Both galaxies are very close to each other in radial distance (22 kpc) (Moretti et al., 2009; De Jong et al., 2010) and also in projected distance on the sky. Their relative radial velocity differs only by about 50 km s^{-1}. Already in the discovery paper of Leo V the authors speculate that the two dwarfs could form a bound pair similar to the Magellanic Clouds. De Jong et al. (2010) argued that to form a bound object the twin system would need a lot of DM, much more than it is seen in similar faint satellites. Nevertheless, the authors claimed that it is highly unlikely that the two satellites are a simple by-chance alignment. They also rule out the possibility that the two faint dwarfs are not galaxies at all but simple density enhancements of a stellar stream by orbital arguments. So they conclude that they might be a 'tumbling pair'. With our paper (see Blaña et al. 2012) we investigate the hypothesis of a bound pair. Using a restricted N-

body code and verifying the results with full N-body simulations, we search for the minimal total mass the system needs, in order to form a tight bound pair.

7.3 Method

1 We adopt a scenario where we model the two galaxies as two dark matter haloes (DMH) orbiting each other. We ignore the luminous components of the galaxies, because their masses are too low to significantly affect their orbits.

2 To restrict the parameter space we adopt two mass-ratios between the two satellites. Using the measured absolute magnitudes, the luminosity ratio between Leo IV and Leo V is 1.8. In our simulations we adopt this ratio for the masses of the two DM haloes as well. We also use scenarios where the ratio is 1, that means that both haloes have the same mass.

3 We proposed two main scenarios for our models as follows:
3.1) *Only radial velocities*: We use only the measured radial velocities, which is the only known component. In the DMH scenario, we also require that the centre of the bigger halo (Leo IV) should not leave the smaller halo (Leo V). This distance (the radius of the smaller halo) is our distance criterion, and ensures a tight bound pair.
3.2) *Radial and tangential velocities*: This scenario is the same as the previous one except that here we add to the galaxies a tangential velocity component to the respective radial velocities. The magnitude of them is as high as the respective radial component. All DMHs are assumed to have a Navarro-Frenk-White (NFW) profile and for each of the cases we vary the concentrations of the haloes in a range usually assumed for the dSph galaxies of $c = 5, 10, 20$.

4 We determine the minimum mass of the system to remain bound using a simple integration code to cover the huge parameter space (Tab.4).

5 Finally we verify the results with full N-body simulations (Tab.4).

In total our investigation produces twelve different solutions to the problem.

7.4 Results & Conclusion

In Tab.4 and Fig.22 (*left panel*) the *total* DM mass for the two faint satellites is shown. Just by looking at our different cases we get results which differ by an order of magnitude in total mass. The values are very high and would put them amongst the most DM dominated objects known. Still these results do not infer that this scenario is impossible. We may see in the left panel of Fig. 22 that the *total* mass does not strongly depend on the concentration of the haloes nor in the mass-ratio between them. But it strongly varies depending on the velocity or kinetic energy they have (scenario with only radial velocity or scenario with

radial and tangential velocity). We compare the masses and M/L-ratios of Leo IV with the values measured by Simon & Geha 2007 within an optical radius of 97pc ($M = 1.4 \pm 1.5 \times 10^6 M_\odot$ and $M/L_V = 78\,[M/L_V]_\odot$). Within the same radius, our models give masses between $5.92 \times 10^5 M_\odot$ and $6.19 \times 10^6 M_\odot$. Similarly, for the M/L-ratios we have a range of $33 - 344\,[M/L_V]_\odot$ respectively. We did the same for Leo V within a radius of 67.4pc with $M = 3.3^{+9.1}_{-2.5} \times 10^5 M_\odot$ and $M/L_V = 75^{+230}_{-58}\,[M/L_V]_\odot$ (Walker et al., 2009a) and we calculated with our models a mass range from $2.7 \times 10^5 M_\odot$ to $2.5 \times 10^6 M_\odot$ and a range of $27 - 250\,[M/L_V]_\odot$ for the M/L-ratios. Furthermore, we checked our results against the trend for dSph galaxies published by Wilkinson et al. (2006) (shown in Fig 22 and in Tab.5), where they calculate the M/L-ratios within a standard radius of 300 pc. Using the same radius, our simulations predict a range for the M/L-ratios $\log_{10} M/L_V = 2.5$–3.7 (See more details for each galaxy in Tab. 5). These values are extremely high but encompass the predictions for dSph galaxies that faint, if an extrapolation of the known values to the faint magnitudes of the Leos is used. The range of observational values allow us to exclude the models with highly concentrated DM haloes ($c = 20$).

The comparison between the results of the restricted and the full N-body simulations show deviations in the distance criterion, but they do not change the outcome of the simulations as it is shown in the eighth column in Tab.4. This distance difference would imply an error in the masses of just 10 per cent and it would not it alter the inferred M/L-ratios significantly. Therefore it does not change our conclusion. A bound pair in the restricted case is still a bound pair in the full simulations.

Summing up, we conclude that the total mass we infer for the system of the Leos to be bound is in fact within a reasonable range of values. Therefore, it could be possible that the two galaxies form a bound pair, making them an ultra-faint counterpart of the Magellanic Clouds.

Table 4: The first column gives the number of the case, the second is the adopted concentration of the haloes. Then we give the mass of the DM halo and its virial radius for Leo IV and Leo V. The next column gives the total masses in DM of the whole system, the next column shows the "ratio" by which the maximum distance differs between the full N-body simulation and the two-body code. The last column is a short explanation for the cases rad. vel. = only radial velocity, rad. & tang. = radial and tangential velocity adopted; mass ratio 1.8 = the two haloes have a fixed mass ratio of 1.8; equal mass = the two haloes have the same mass.

Case	c	$M_{DM,LeoIV}$ [$M_\odot$]	$r_{vir,LeoIV}$ [kpc]	$M_{DM,LeoV}$ [$M_\odot$]	$r_{vir,LeoV}$ [kpc]	M_{tot} [$M_\odot$]	Ratio	Scenario
0a	—					4.18×10^9	–	Point masses (a)
0b	—					1.47×10^{10}	–	Point masses (b)
1	5	1.34×10^{10}	49.00	7.45×10^9	40.29	2.09×10^{10}	0.965	rad. vel. mass ratio 1.8
2	10	1.27×10^{10}	48.11	7.05×10^9	39.55	1.98×10^{10}	0.953	rad. vel. mass ratio 1.8
3	20	1.22×10^{10}	47.42	6.75×10^9	39.98	1.89×10^{10}	0.935	rad. vel. mass ratio 1.8
1a	5	9.05×10^9	42.99	9.05×10^9	42.99	1.81×10^{10}	1.179	rad. vel. equal mass
2a	10	8.55×10^9	42.18	8.55×10^9	42.18	1.71×10^{10}	1.194	rad. vel. equal mass
3a	20	8.30×10^9	41.76	8.30×10^9	41.76	1.66×10^{10}	1.204	rad. vel. equal mass
4	5	3.47×10^{10}	67.25	1.93×10^{10}	55.28	5.39×10^{10}	0.993	rad. & tang. vel. mass ratio 1.8
5	10	3.11×10^{10}	64.83	1.73×10^{10}	53.30	4.14×10^{10}	0.956	rad. & tang. vel. mass ratio 1.8
6	20	2.84×10^{10}	62.90	1.58×10^{10}	51.70	4.42×10^{10}	0.968	rad. & tang. vel. mass ratio 1.8
4a	5	2.40×10^{10}	59.50	2.40×10^{10}	59.50	4.80×10^{10}	1.450	rad. & tang. vel. equal mass
5a	10	2.20×10^{10}	57.80	2.20×10^{10}	57.80	4.40×10^{10}	1.375	rad. & tang. vel. equal mass
6a	20	2.10×10^{10}	56.91	2.10×10^{10}	56.91	4.20×10^{10}	1.284	rad. & tang. vel. equal mass

Table 5: Mass-to-light ratios within a radius of 300 pc. **Note**: We adopt V-band magnitudes of -5.8 for Leo IV and -5.2 for Leo V.

Case	1	2	3	1a	2a	3a	4	5	6	4a	5a	6a
c	5	10	20	5	10	20	5	10	20	5	10	20
LeoIV: Log_{10} ($M_\odot/L_\odot$)	2.544	2.929	3.343	2.484	2.867	3.279	2.686	3.067	3.482	2.631	3.014	3.425
LeoV: Log_{10} ($M_\odot/L_\odot$)	2.710	3.092	3.499	2.740	3.122	3.534	2.853	3.232	3.641	2.886	3.270	3.688

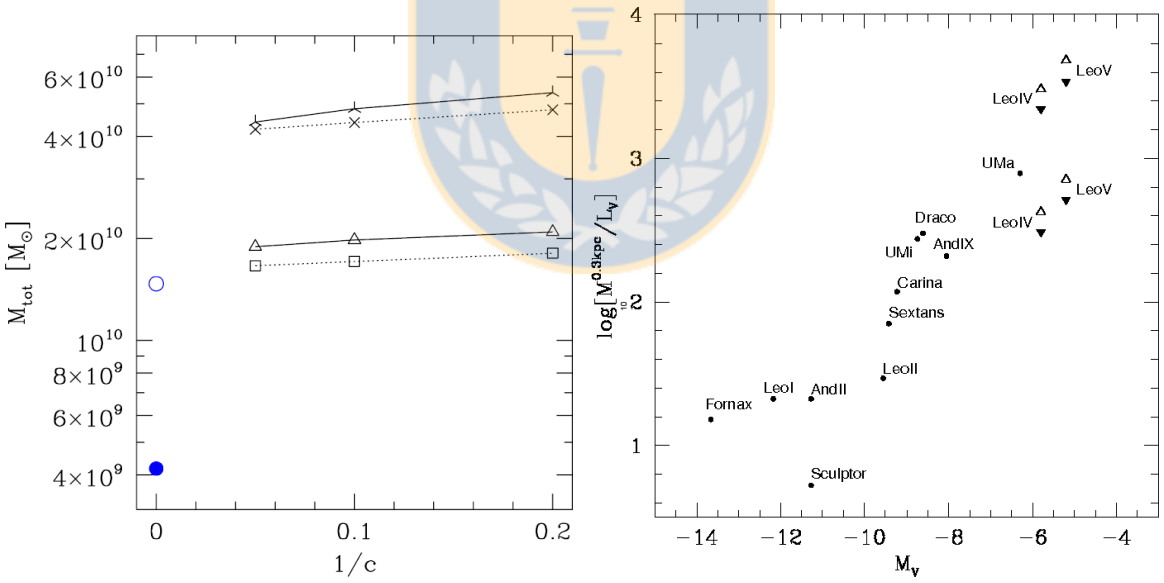

Figure 22: *Left:* Minimum DM mass of the total system M_{tot} versus concentration of the haloes. We plot $1/c$ in favour of c to include the point-mass results at $1/c = 0$ (cases 0a,b; plotted as open and filled circle - blue online). Solid lines are the results using the mass-ratio 1.8. Triangles are cases with radial velocity only and tri-stars with additional tangential velocity. Dashed lines show the results of equal mass haloes. Squares are radial-velocity-only cases and crosses have additional tangential velocity. *Right:* Mass-to-light ratios within a radius of 300 pc. The circles are dSph Galaxies of the Local Group as reported by Wilkinson et al. (2006). For Leo IV, the filled upside-down triangles are cases 1a and 3 (concentrations $c = 5$ and $c = 20$ respectively) with radial velocities only. The open triangles are cases 4a and 6 ($c = 5$ and $c = 20$) with radial and tangential velocities. For Leo V we plot the values of cases 1 and 3a as well as 4 and 6a, respectively. We use these specific cases because they span the whole range of our results.

8 Bibliography

References

Allison R.J., et al., 2009, MNRAS, 395, 1449

Allison R.J., Goodwin S.P., Parker R.J., de Grijs R., Portegies Zwart S.F., Kouwenhoven M.B.N., 2009, ApJ, 700, L99 - L103, 2009

Allison R.J., Goodwin S.P., Parker R.J., Portegies Zwart S.F., de Grijs R., 2010, MNRAS, 407, 1098

Adams F.C., Myers P.C., 2001, ApJ, 553, 744

Bastian N., Goodwin S.P., 2006, MNRAS, 369, L9

Bate, M. R., 2009, MNRAS, 392, 590-616

Bate, M. R., 2011, MNRAS, 418, 703-704

Baumgardt H. and Kroupa P., 2007, MNRAS, 380, 1589

Belokurov V., et al. 2007, ApJ, 654, 897

Belokurov V., et al. 2008, ApJ, 686, L83

Binney J., & Merrifield M., 2008, Princeton Univ. Press, Galactic Astronomy, 1st ed

Binney J., & Tremaine S., 2008, Princeton Univ. Press, Galactic Dynamics, 2nd ed.

Boily C.M., Kroupa P., 2003a, MNRAS, 338, 665

Boily C.M., Kroupa P., 2003b, MNRAS, 338, 673

Bonnell I.A., Bate M.R., 2006, MNRAS, 370, 488

Bonnell I.A., Bate M.R., 2006, MNRAS, 370, 480

Bonnell I.A., Smith R.J., Clark P.C., Bate M.R., 2011, MNRAS, 410, 2339

Bressert E., et al., 2010, MNRAS, 409, L54

Chen L., de Grijs R., & Zhao J.L., 2007, AJ, 134, 1368

Chomiuk L., Povich M., 2011, AJ, V142, I6, 197, 16 pp

De Jong J.T.A., Martin N.F., Rix H.-W., Smith K.W., Jin S., Macciò A.V. 2010, ApJ, 710, 1664

Elmegreen B.G., Clemens C., 1985, ApJ, 294, 523

Elmegreen B.G., Elmegreen D.M., 2001, AJ, 121, 1507

Farias J.P., in prep

Fellhauer M., Kroupa P., 2002, MNRAS, 330, 642

Fellhauer M., Kroupa P., 2002b, AJ, 124, 2006

Fellhauer M., Wilkinson M. I., Kroupa P., 2009, MNRAS, 397, 954

Geyer M.P., Burkert A., 2001, MNRAS, 323, 988

Guzmán A.E., Garay G., Brooks K.J., Voronkov M.A., 2012, ApJ

Goodwin S.P., 1997a, MNRAS, 284, 785

Goodwin S.P., 1997b, MNRAS, 286, 669

Goodwin S.P., Whitworth A., 2004, A&A, 413, 929

Goodwin S.P., 2009, Ap&SS, 324, 259

Gutermuth R.A., et al., 2009, ApJS, 184, 18

Harris W. E., 1996, AJ, 112, 1487

Hills J.G., 1980, ApJ, 235, 986

Illingworth G. 1976, ApJ, 204, 73

Klessen R.S., 1997, MNRAS, 292, 11

Kroupa P., 2001, MNRAS,322, 231-246

Lada C.J., Lada E.A., 2003, ARA&A, 41, 57

Mac Low M.M., 1999, ApJ, 524, 169

Moretti M.I., et al. 2009, ApJ, 699, L125

Parmentier G., Goodwin S.P., Kroupa P., Baumgardt H., 2008, ApJ, 678, 347

Preibisch T., *http://www.usm.uni-muenchen.de/people/preibisch/*

Sand D.J., Seth A., Olszewski E.W., Willman B., Zaritzky D., Kallivayalil N. 2010, ApJ, 718, 530

Simon J.D., Geha M. 2007, ApJ, 670, 313

Simon J.D.,Frebel A., McWiliam A., Kirby E.N., Thompson I.B. 2010, ApJ, 716, 446

Smith et al., 2012

Smith R., Slater R., Fellhauer M., Goodwin S., Assmann P., 2011a, MNRAS, 414, 3036

Smith R., Fellhauer M., Goodwin S., Assmann P., 2011b, MNRAS, 416, 383

Spitzer L.J., 1969, ApJ, 158, L139

Spitzer L.J., 1987, Dynamical Evolution of Globular Clusters

Stahler, 2012

Verschueren W., David M., 1989, A&A, 219, 105

Walker M.G., Belokurov V., Evans N.W., Irwin M.J., Mateo M., Olszewski E.W., and Gilmore G. 2009, ApJ, 694, L114

Walker M.G., Mateo M., Olszewski E.W., Penarrubia J., Evans, N.W., Gilmore G. 2009, ApJ, 704, 1274

Weidner C., Kroupa P., 2004, MNRAS, 348, 187

Weidner C., Kroupa P., Nürnberger D.E.A., Sterzik M.F., 2007, MNRAS, 375, 673

Weidner C., Kroupa P., & Bonnell I.A.D., 2010, MNRAS, 401, 275

Willman M.I., Kleyna J.T., Gilmore G.F., Evans N.W., Koch A., Grebel E.K., Wyse R.F.G., Harbeck D.R. 2006, Msngr, 124, 25

Wilkinson M.I., Kleyna J.T., Gilmore G.F., Evans N.W., Koch A., Grebel E.K., Wyse R.F.G., Harbeck D.R. 2006, Msngr, 124, 25

Zucker D.B., et al. 2006, ApJ, 643, L103

9 Acknowledgments

Mis agradecimientos a la Universidad de Concepción por la beca de articulación que se me otorgó para el Magíster durante el 2011.
También agradezco a CONICYT por financiarme para realizar el Magister mediante su BECA-CONICYT durante el periodo Abril 2012 hasta Febrero 2013. Su ayuda me permitió tener una dedicación exclusiva a realizar mi Magister.
También agradezo al Director Doug Geisler y al Departamento de Astronomía por su apoyo con el BASAL PFB-06/2007 "Centro Chileno de Excelencia en Astrofísica y Tecnologías Afines (CATA), durante el segundo semestre del 2013.
Agradezco al Profesor Michael Fellhauer por su apoyo para mi Tesis mediante el FONDECYT 1130521 durante el final del primer semestre 2013.

Mas me gustaría reiterar el agradecimiento que hice para mi tesis del Título Profesional, pues mi etapa de Magister y término del pregrado fueron en realidad la misma. Mediante esta segunda tesis concluyo esta importante etapa de mi vida, pero no lo hago solo pues numerosas personas estuvieron involucradas en mi formación profesional y por sobre todo personal. Es la punta de un iceberg de bastantes años de inolvidables y olvidables experiencias. Mi elección de la Ciencia como centro de mi atención profesional trasciende hacia el plano personal, hacia un plano filosófico de índole metafísico. Y la Astronomía con su cosmovisión macroscópica, empírica y teórica me entrega precísamente eso, y agradezco profundamente a todas las personas que contribuyeron para que pudiera seguir este camino.

Y todo esto no hubiera sido posible de no ser por personas como mis amados padres, *Claudio Blaña de la Cruz* y *Ana Díaz Aliste*, quienes con su apoyo constante e incondicional me ayudaron a seguir este hermoso camino. Les estaré agradecido hasta la eternidad por todos sus años de esfuerzo. También agradezco de profundo corazón a mis hermanos que son casi mis segundos padres, *Claudio Blaña Díaz* y *Heidi Blaña Díaz*, por su constante apoyo. Extiendo también mis agradecimientos a toda mi familia, a mis abuelas Omi, la Abue y abuelos, tios, primos, cuñados y sobrinos por esos momentos felices. Agradezo a mi querida y bella polola *Carolina Agurto Gangas* por su apoyo, paciencia y cariño durante esta etapa.

También agradezco a la *Burschenschaft Montania* y a todos sus miembros por todos estos años de grandiosas experiencias y recuerdos. Dichas experiencias me entregaron la comprensión de la importancia de los ideales como guías: *Ehre, Freundschaft und Recht* y de lo difícil que es plasmarlas y mantenerlas en la *realidad*: *"Die Ideale sind ein Leuchtturm, kein Hafen"*. Por ello agradezo profundamente a mis *Bundesbrüder*: *Schiffer, Allenthao, Jako, Droopy, Manta, Zerstörer, Wethy Wop, Schokolade, Skatmann, Bisbald, Kayeukhe, Leeche, Nachteule, Sechsa Piehl, Dihazepahm, Leopard, Galgho, Zombie, Neohpren, Malignuss, Malditus, Parvulito, Simon, Frosch, Lavin, Osram y muchos más.*

También agradezco a todos eso amigos que la vida (y el terremoto) me trajo, *Robert, Nestor, Urzula, Annette, Ciro, Rhodia, Gustavo* y muchos más, junto a los cuales tuve intere-

santes conversaciones como con el grupo de los *Cangrejos*.

Agradezo a mis profesores del colegio, en especial al *Profesor Luis González*, por todas esas charlas sobre física en los recreos, que reforzaron mi interés por la Ciencia.

También agradezco a la *Universidad de Concepción* y a toda la gente que ahí trabaja. El carácter laico, académico y de vocación social de esta universidad ayudaron a forjarme un espírutu con dichos atributos. Y a la gente que conocí en esta etapa les doy las gracias; a mis compañeros de universidad y amigos astronómico que conocí en conferencias, por todos esas noches de estudio y festejos, tanto de la vieja carrera de CFA como de la nueva carrera de Astronomía: *Mairon, Pamela, Coté, Roy, Fabián, Fede, Gustavo O., Gustavo A., Bego, Carolina S., Leonardo, Daniela, Rodrigo, Mónica, Caddy y César* entre otros. Agradezco al Departamento de Física, donde se formaron mis bases académicas.y a sus profesores *Dr. Jaime Araneda, Dr. Claudio Faúndez, Dr. Joaquín Díaz de Valdéz, Dr. Paulraj Manidurai, Dr. Guillermo Rubilar, Dr. Patricio Salgado, Dr. Rolando Hernández* y a muchos más.
Y al Departamento de Astronomía y sus profesores Doug Geisler, Dr. Ricardo Demarco, Dr. Wolfgang Gieren, Dr. Ronald Mennickent y especialmente a los profesores de mi comisión; al *Dr. Sandro Villanova*, y muy especialmente al *Dr. Neil Nagar* por todos esos años de clases que siempre ha realizado mostrando gran simpatía y un gigantezco compromiso con sus estudiantes, les estaré siempre agradecido. Y agradezco también a la señora *Jeanette Espinoza*, a don *Victor Mora* y en especial a la señora *Marcela Sanhueza* por cuidarnos maternalmente todos estos años de pregrado, defendiendonos de la burocracia, y a *Ronald Burgos* por salvar a mi computador tantas veces. Agradezco también a los doctorandos y postdoctorados, *Richard Lane*, *André-Nicolas Chené*, *Roger Leiton*, *Ricardo Bustos*, *Renee Mateluna*, *Francesco Mauro*, *Bogumil Pilecki*, *Hugo Messias* y *Paulina Assmann* por el conocimiento tanto científico como de la vida del científico que compartieron conmigo. Le extiendo un especial agradecimiento al grupo de teoría por sus aportes en mi formación científica: Al *Dr. Rory Smith* por todas esas discusiones interesantes y su gran apoyo para realizar posters y charlas en conferencias. Estoy seguro que los nuevos integrantes del grupo, *Juan Pablo Farías* y el *Dr. Graeme Candlish* aprenderán y aportarán mucho al grupo. A ellos también les agradezco por su gran ayuda. Y muy especialmente agradezco al Profesor *Dr. Michael Fellhauer*, por confiar y potenciar mis habilidades y por su gran compromiso como profesor supervisor, permitiéndome desde el comienzo realizar interesantes proyectos de investigación que concluyeron con publicaciones en revistas reconocidas. Y por apoyar e incentivar mi participación en conferencias nacionales e internacionales y en general por darle un gran empuje a mi carrera profesional, le estaré eternamente muy agradecido.

Mas el pasado y el presente se reúnen en este trabajo para mirar hacia un futuro de posibilidades. Un ciclo ha concluido, pero muchos más habrán de venir.

A todos les doy mis más sinceros agradecimientos,

Matías Andrés Blaña Díaz